

Atomic and Electronic Structure of the Clean and Adsorbate Covered (0001) Surface of the Topological Insulator Bi_2Se_3

Holger L. Meyerheim* and Christian Tusche

We review recent progress in the characterization of the atomic and electronic structure of pristine and adsorbate-covered $\text{Bi}_2\text{Se}_3(0001)$ using state-of-the-art analysis tools like surface X-ray diffraction, X-ray absorption fine structure, and spin- and momentum-resolved photoemission spectroscopy. On the basis of several examples we show how the topological surface state is modified by structural modifications. One example is the shift of the Dirac point of the pristine $\text{Bi}_2\text{Se}_3(0001)$ surface induced by trace amounts of carbon and its concomitant expansion of the topmost inter-layer spacing. Dosing with atomic hydrogen leads to the complete removal of selenium within the top quintuple layer leaving behind a bismuth bilayer on selenium-terminated $\text{Bi}_2\text{Se}_3(0001)$ thereby leading to the appearance of hole-like Rashba-split surface states. Gold deposited by molecular beam epitaxy substitutes bismuth within the near surface region involving an opening of a gap in the topological surface state.

1. Introduction

Topological insulators (TI) represent an unusual state of matter. While they are insulators in the bulk their surface is metallic owing to a surface state which is spin polarized and topologically protected by time reversal symmetry. Prototype phases are the chalcogenides of bismuth and antimony such as Bi_2Se_3 , Bi_2Te_3 , and Sb_2Te_3 . Owing to its large bulk band gap of the order of 0.3 eV, $\text{Bi}_2\text{Se}_3(0001)$ has been intensely studied in the past. One key issue is that that the topological protection can be lifted by a magnetic field oriented perpendicular to the surface involving an opening of a gap at the Dirac point (D_P) which is decisive for the realization of exotic quantum effects such as the quantum anomalous Hall effect. To this end TIs were *bulk* doped by

magnetic species such as iron, chromium, and manganese in order to create a ferromagnetic (FM) ordering.^[1–12] Bulk dopants typically reside in substitutional sites, i.e., they replace bismuth atoms within the structure.^[4,7,8,10,13,14] Bulk doping is, however, limited to a concentration of about 5–10% only. In general, this limitation can be overcome by surface doping, which is well known to allow metastable structures in the ultra-thin film limit. In our research, we have followed this approach by depositing different atomic species in situ under ultra-high-vacuum conditions using molecular beam epitaxy and—in the case of atomic hydrogen—by using a radio frequency plasma source.^[15–18] The geometric structures were analyzed by surface X-ray diffraction (SXRD) and by X-ray absorption fine structure (XAFS) experiments complemented by scanning

tunneling microscopy (STM), while the electronic structure was investigated by state-of-the-art spin-resolved momentum microscopy. In the following, we discuss several recent examples beginning with the investigation of the pristine $\text{Bi}_2\text{Se}_3(0001)$ surface followed by two examples representative for substitution processes involving selenium (dosing by atomic hydrogen) and bismuth atoms (gold) deposition.

2. X-Ray Structure Analysis Applied to Surfaces

The SXRD data collection was carried out at the Max-Planck-Institute in Halle using an in-house ultra-high vacuum (UHV) diffractometer and at the beamline 25b of the European Synchrotron Radiation Facility (ESRF) in Grenoble (France). In all cases, data collection is carried out by employing a two-dimensional (2D) pixel detector. For the in-house experiments a microfocus X-ray source (Cu-K_α) was used. In order to outline the basic principle of the structure analysis in **Figure 1** a schematic of the reciprocal space in an a^*c^* section is shown together with the corresponding crystal which is *semi-infinite* along the c -axis. Therefore, in addition to the bulk Bragg-points (spheres), there exist rods normal to the sample surface which are shown as thin solid lines (in the schematic no surface miscut is assumed, thus the rods run parallel to c^* defined by the bulk lattice). These rods are referred to as “crystal truncation rods” (CTRs). They were already theoretically predicted by von Laue in 1936,^[19] but the first clear-cut experimental verification took

Dr. H. L. Meyerheim
Max-Planck-Institut für Mikrostrukturphysik Halle
Weinberg 2, D-06120 Halle, Germany
E-mail: holger.meyerheim@mpi-halle.mpg.de

Dr. C. Tusche
Forschungszentrum Jülich GmbH
Peter Grünberg Institut (PGI-6), D-52425 Jülich, Germany
E-mail: c.tusche@fz-juelich.de

Dr. C. Tusche
Fakultät für Physik
Universität Duisburg-Essen
D-47057 Duisburg, Germany

DOI: 10.1002/pssr.201800078

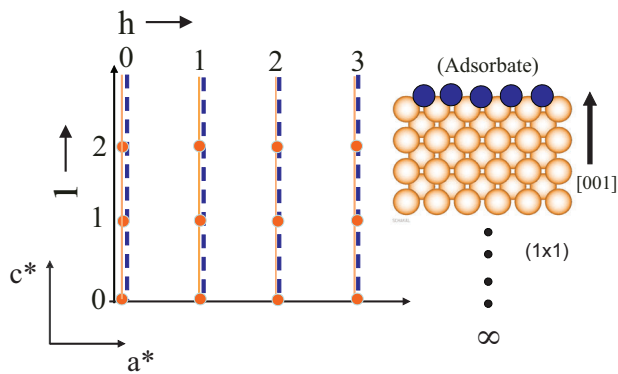


Figure 1. Schematic of the reciprocal space in an a^* - c^* section. The corresponding crystal structure is shown in the right. Bulk Bragg reflections of the semi-infinite crystal are represented as spheres at integer positions h and ℓ . The truncation of the crystal gives rise to rods along c^* (solid line). Adsorption involves a coherent addition of the scattering amplitudes between the rods of the substrate and those of the adsorbate, the latter represented by the dotted lines.

until 1986 published by Robinson.^[20] The detailed calculation shows that in the case of a bulk truncated crystal, the intensity along the CTRs varies by roughly five orders of magnitude between the in-phase bulk Bragg positions at integer ℓ and the anti-phase condition half way between the Bragg-reflections. Consequently, at the anti-phase condition, where the reflected intensity of a semi-infinite fcc-type crystal is calculated to be equal to that of a quarter of a monolayer, adsorption of foreign species substantially modifies the total reflected intensity.

The structure factor amplitude of a primitive crystal can be written as the semi-infinite sum over the lattice planes from $-\infty$ to zero:

$$F_{\text{CTR}} = \sum_{n=-\infty}^0 \exp [2i\pi\ell n] \times g(h) \times g(k) \quad (1)$$

$$= \frac{1}{1 - \exp[-i2\pi\ell]} \times g(h) \times g(k) \quad (2)$$

where the atomic scattering amplitude (f) and the finite penetration of the X-ray beam were neglected. The latter, expressed by an effective absorption factor $\exp[-\mu \times n \times d]$ (with d the layer spacing and μ the absorption coefficient) lifts the divergence of the lattice sum at the bulk Bragg conditions at integer ℓ . We have explicitly considered only the summation along the z -direction (surface normal) and included the contributions along the a and b direction in the “Laue factors” $g(h)$ and $g(k)$.^[19] Adsorption of any species as well as relaxations of the substrate can be simulated by coherent addition of F_{CTR} with the adsorbate amplitude to give the total scattering amplitude (F_{tot}) which can be expressed by:

$$F_{\text{tot}} = F_{\text{CTR}} + \sum_j f_{\text{ad}} \times \theta_j \times \exp [i2\pi(hx_j + ky_j + \ell z_j)] \quad (3)$$



Holger L. Meyerheim graduated from the Ludwig-Maximilians-Universität (LMU) in Munich (Germany) in 1985 in Mineralogy and Crystallography. He completed his doctorate in experimental physics at the Freie Universität Berlin in 1990. For his thesis he was awarded with the Ernst-Eckhard-Koch prize. In 1990, he moved to

LMU to become Wissenschaftlicher Assistent where he established the surface X-ray diffraction group at the Institut für Kristallographie & Mineralogie. In 1995 he completed his “Habilitation” (Dr. rer. nat. habil.). In 1999, he joined the Max-Planck-Institut für Mikrostrukturphysik in Halle (Germany) where he is now group leader and “Privatdozent” at the Martin-Luther-University Halle-Wittenberg.



Christian Tusche carried out his doctoral studies at the Max-Planck-Institute of Microstructure Physics in Halle, Germany, and received his doctorate in experimental physics from the University Halle-Wittenberg in 2007. In the following years, he became the leading scientist of the spin-resolved photoemission group at the Max-Planck-Institute of

Microstructure Physics. Form 2015, he became a senior scientist at the Peter Grünberg Institute at the Forschungszentrum Jülich and a member of the Faculty of Physics at the University Duisburg-Essen. In 2016, he has been awarded the Innovation Award on Synchrotron Radiation for his development of “Imaging Spin-Filters for Spin-Resolving Momentum Microscopy.”

with the atomic scattering factor f_{ad} of the adsorbate and its fractional coverage θ . The summation runs over all atoms j within the surface unit cell. In summary, surface structure determination by X-ray diffraction is based on the collection and simulation of reflections originating from the surface termination or—in the case of superstructures—from the appearance of isolated rods in reciprocal space. This can be viewed as a “Fourier filtering” selecting the proper information in k -space. Experimentally, data collection is often carried out by grazing incidence of the incoming beam (e.g., under external total reflection conditions at a critical incidence angle $\alpha_c = 0.3^\circ$ for Cu- K_α radiation) which is favorable to reduce to diffuse background due to thermal diffuse scattering from the bulk. It should be emphasized, however, that this is not contributing to what is referred to as “surface sensitive” since the characteristic decay length (Λ) of the X-ray beam in the crystal is of the order of 10 nm, even under total reflection conditions.

3. Momentum- and Spin-Resolved Photoemission Spectroscopy

Photoelectron spectroscopy is nowadays recognized as a very powerful tool to study detailed electronic structures of solid surface. Since the photon has a well-defined energy $h\nu$ information on the initial electronic states can be directly derived due to the energy- and momentum-conservation rules and optical selection rules. In the simplest case, the experimentally measured photoemission intensity is usually described by Fermi's golden rule

$$I_{h\nu} \sim |\langle \psi_f | M_{if} | \psi_i \rangle|^2 \cdot \delta(E_f - E_i - h\nu) \quad (4)$$

where ψ_i is the initial state wave function with binding energy E_i and (ψ_f, E_f) the photoexcited final state, respectively. The “ δ ” term in Equation (4) expresses the law of energy conservation. Thus, a photoemission spectroscopy experiment directly yields information on the binding energy of electronic states. The surface sensitivity of the photoemission experiment is determined by the inelastic mean free path of electrons in the solid, i.e., the escape depth of electrons before they undergo inelastic scattering. For inorganic compounds the highest surface sensitivity is typically found at a kinetic energy of about $E_{kin} = 50$ eV to be of the order of 5–10 Å.^[21] For Bi₂Se₃(0001) this means that most of the photoemission signal originates from the topmost quintuple layer (QL).

In many cases, the final state of the photoemission process can be assumed to be a free electron like state,^[22] and useful estimates of the matrix element M_{if} in Equation (4) can be drawn.^[23] The photoexcited electron in the solid has the wave vector \mathbf{k} which can be decomposed into the parallel (\parallel) and the perpendicular component (\perp) with $k_{f,\parallel} = k_{i,\parallel} + G_{\parallel} + q_{\parallel}$ and $k_{f,\perp} = k_{i,\perp} + G_{\perp} + q_{\perp}$, where f and i stand for the final and initial states and G for the reciprocal lattice vector. Here, \mathbf{q} is the wave-vector of the photon, which can be neglected for excitation energies in the UV to VUV range. Most importantly, the translation invariance of a crystalline solid for translation vectors within the surface plane leads to the conservation law of the transverse crystal momentum coordinate, k_{\parallel} . As illustrated in **Figure 2**, the component of electron momentum vector parallel to the surface is therefore conserved during the photo excitation

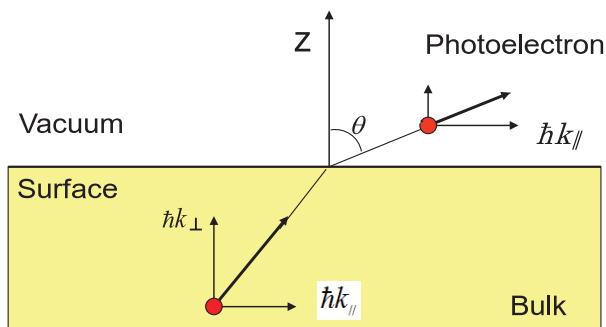


Figure 2. Schematic of the photoemission of an electron at a surface. Only k_{\parallel} (parallel to the surface) is conserved on the escape of photoelectrons into the vacuum.

and the subsequent emission of the photoexcited electron to the vacuum.

Angular resolved photoemission spectroscopy (ARPES) measures the energy and the emission angle θ of the photoelectron from the solid, and thus can directly derive the crystal momentum k_{\parallel} . Surface states, and in particular the topological surface state (TSS) of Bi₂Se₃ or other TIs, are two-dimensional (2D) electronic states. As such, they are only characterized by two in-plane momentum coordinates (k_x, k_y), while the perpendicular momentum coordinate k_{\perp} is not a good quantum number. An ARPES experiment is therefore directly suitable for a complete characterization of these surface states. To some extent this also applies to bulk states of quasi 2D materials like Bi₂Se₃, where 2D QLs only weakly interact across the VdW gap.

We have carried out momentum-resolved photoemission experiments using a home built momentum microscope.^[24] The experimental setup is outlined in **Figure 3**. Photoelectrons emitted into the complete solid angle above the sample surface were collected by the objective lens of a photoelectron emission microscope. Since an electric field of a few kV mm^{-1} is applied between the sample surface and the entrance of the momentum microscope, the angle θ of the emitted photoelectrons is transformed such that

$$\sin \theta = \sin \theta' \sqrt{\frac{eU_A}{E} + 1} \quad (5)$$

when entering the momentum microscope. When the acceleration voltage U_A is large compared to the energy E of the photoelectrons this is simplified to $\sin(\theta) = k_{\parallel}$, and the resulting image is scaled linear as a function of the lateral crystal momentum coordinates (k_x, k_y). We note that this is different compared to typical ARPES experiments that measure θ , but not

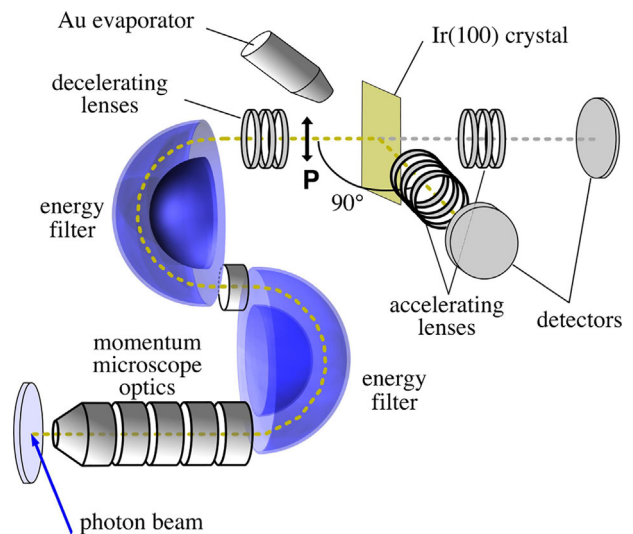


Figure 3. Momentum microscope setup with imaging electron optics, energy filter, and detection branches for spin-integral and spin-filtered momentum images. Recording of 2D spin-filtered images is accomplished by reflection of photoelectrons at the Ir(100) crystal inserted after the energy filter.

directly k_{\parallel} . Series of constant energy momentum images, energy filtered using an electrostatic analyzer, are then recorded by a CCD camera from a fluorescent screen detector.

For spin-resolved momentum microscopy measurements, a Ir(100) single crystal is introduced into the momentum microscope, such that electrons are specularly reflected at the crystal surface such that the 2D momentum image is preserved.^[25] Electrons reflected from the crystal surface undergo spin-dependent scattering. The recorded intensity on the spin-resolving image detector branch depends on the electron spin being aligned parallel or antiparallel to the vertical quantization axis (see Figure 3). For reflection from a Ir(100) surface passivated by one monolayer (ML) of gold atoms this scattering asymmetry can reach up to 65%.^[26] A quantitative measurement of spin-up and spin-down partial intensities is achieved by variation of the scattering asymmetry by changing the scattering energy,^[24,26] and data are analyzed according to ref. [27].

The Bi_2Se_3 single crystal was illuminated by He-I ($h\nu = 21.23$ eV) radiation from a focused gas discharge lamp (UVS300, Specs), under an angle of incidence of 22° with respect to the sample surface, or by the fourth harmonic ($h\nu = 6.0$ eV) of a mode locked Ti:Sa oscillator. In the case of laser illumination, the polarization plane of the light can be tuned to be either s- or p-polarized with respect to the sample surface, while the He-I radiation is unpolarized.

4. The Pristine Bi_2Se_3 (0001) Surface

4.1. SXRD of Pristine and Carbon-Doped Bi_2Se_3 (0001)

Despite an abundance of studies concerning the presence of the TSS in Bi_2Se_3 (0001) surprisingly scarce was the knowledge of the atomic surface structure. Bulk Bi_2Se_3 crystallizes in the tetradymite ($\text{Bi}_2\text{Te}_2\text{S}$) structure which has a rhombohedral symmetry [space group $D_{3d}^5(R\bar{3}2/m)$], with lattice parameters being equal to $a_0 = 4.14$ Å and $c_0 = 28.64$ Å in the hexagonal setting. The atomic structure was analyzed in several studies in the past.^[28–30] The basic building block is a QL which is characterized by a sequence of Se-Bi-Se-Bi-Se atomic planes which are stacked in an ABCA . . . sequence (see Figure 4). Thus the hexagonal unit cell contains three QLs. The QLs are connected by weak van der Waals (vdW) bonds, which make these crystals easily cleavable.^[31] Since there is considerable scatter in the atomic structure parameters for bulk Bi_2Se_3 in the first step we have carried out a structure analysis of a Bi_2Se_3 powder based on the Bragg–Brentano method using Mo- K_α radiation ($\lambda = 0.7092$ Å). Data were fitted by using the Rietveld analysis method and the results are listed in Table 1.

The (0001) surface can be easily prepared by crystal cleaving leading to a bulk-truncated surface exposing the top selenium layer. However, this view was challenged by a low energy ion scattering study which proposed a bismuth bi-layer termination,^[32] but a later low energy electron diffraction (LEED) analysis of the very similar phase Bi_2Te_3 ^[33] and of Bi_2Se_3 ^[34] found evidence for a single tellurium or selenium termination, respectively. This situation called for a thorough analysis of the Bi_2Se_3 (0001) surface using SXRD.^[35,36]

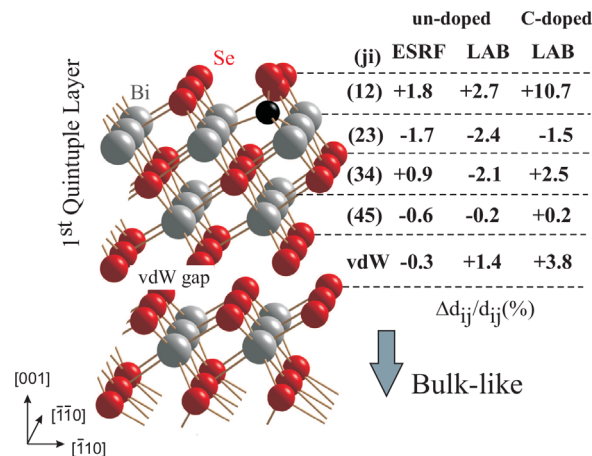


Figure 4. Model of the Bi_2Se_3 near-surface structure. Red (small) and gray (large) spheres represent Se and Bi atoms, respectively. Interlayer spacings relative to the bulk are labeled on the right for the different data sets. Carbon (small black sphere) is placed in the most favorable position according to ab initio calculations. Reprinted figure with permission from ref. [15]. Copyright (2014) by the American Physical Society.

In the present work, the bulk single crystals were prepared by mild Ar^+ ion sputtering followed by annealing at about 480°C for about 30 min, which results in a clean surface as evidenced by Auger electron spectroscopy (AES) and a well-contrasted LEED pattern.^[15,16] Carbon contamination could not be detected on the basis of the AES spectra, however, based on the SXRD analysis in combination with ab initio calculation it

Table 1. Summary of the Rietveld powder diffraction analysis of bulk Bi_2Se_3 . In space group $R\bar{3}2/m$ (no. 166) Bi and Se atoms occupy Wyckoff positions 3a at (0, 0, 0) and 6c at (0, 0, z). Data reproduced from ref. [16].

Data collection		
Wavelength	0.70922 Å (Mo-K α)	
2 θ range	5–45°	
2 θ step	0.02°	
Lattice parameters		
Space group	$R\bar{3}m$	
a (Å)	4.13988 (2)	
b (Å)	4.13988 (2)	
c (Å)	28.644 (2)	
V (Å ³)	425.1	
Atomic coordinate	(z)	B-factors (Å ²)
Bi ₁ (6c)	0.4011 (2)	1.42 (0.08)
Se ₁ (3a)	0.0000	0.73 (0.36)
Se ₂ (6c)	0.2102 (3)	0.68 (0.16)
Reliability factors		
R _{Bragg}	9.6%	
R _p	15.7%	
χ^2	3.8	

was concluded that trace amounts of carbon resides in interstitial octahedral sites (see Figure 4).

Several CTRs of the pristine (0001) surface of a Bi_2Se_3 single crystal are shown in Figure 5. Calculated ($|F_{\text{calc}}(hk\ell)|$) structure factor amplitudes (lines) are compared with collected data ($|F_{\text{obs}}(hk\ell)|$) shown as symbols. Panels (a) and (b) correspond to data collected at the ESRF (a) and using the in-house laboratory setup (LAB) (b), respectively. The structure factor amplitudes were derived from integrated intensities $|F_{\text{obs}}(hk\ell)| \propto \sqrt{I(hk\ell)}$ collected under grazing incidence [$\alpha_i = 0.3^\circ$ (LAB) and $\alpha_i = 1.0^\circ$ (ESRF)] of the incoming beam. Details about the instrumental correction factors can be found in refs. [37–39]. According to the rhombohedral space group symmetry ($R\bar{3}2/m$) in its hexagonal setting, bulk Bragg reflections appear at the condition $-h + k + \ell = 3n$ ($n \in \mathbb{Z}$). It is already evident by direct inspection that the data collected at the ESRF closely resemble those collected in the laboratory. One complete data set of the latter consists of about 160 symmetry independent reflections. The ESRF data set consists of 1079 reflections along five CTRs.

The structure refinement was carried out by least squares fit allowing the vertical positions of the atoms within the first QL to vary. Owing to the high site symmetry of the atomic species in the two-dimensional space group $p3m1$ with only one selenium

or bismuth in each layer, only the z -parameters of the atoms are free structural parameters. In addition, the displacement factor $T(q)$ representing thermal and static disorder was varied in each layer. It is given by $T(q) = e^{-B \cdot q^2/4}$, where q is the magnitude ($q = 2 \times k \times \sin\theta$) of the scattering vector and B represents the Debye-parameter given by $B = 8\pi \langle u^2 \rangle$ where $\langle u^2 \rangle$ is the mean squared displacement amplitude. For details we refer to refs. [40,41]. In SXR D the fit quality can be quantified by several parameters, one of them being the un-weighted residuum (R_u).^[42] For the structure model discussed below a good fit with $R_u = 12\%$ is obtained. Another quality parameter is the goodness of fit (GOF). It is given by: $\text{GOF} = \sqrt{1/(N - P) \cdot \sum [(I_{\text{obs}} - I_{\text{calc}})^2 / \sigma^2]}$,^[43] where the difference between observed and calculated intensities is normalized to the uncertainties expressed by the standard deviation (σ) and to $(N - P)$, i.e., the difference between the number of independent data points (N) and the number of parameters (P) which are varied. For the evaluation of the GOF, the correct estimate of the total uncertainties (1σ) of the $|F_{\text{obs}}(hk\ell)|$ represented by the error bars in Figure 5 is of utmost importance to obtain meaningful results. In general, σ is calculated by the quadrature sum of the statistical and the systematic uncertainty (see e.g., ref. [44]). For the data sets shown in Figure 5 we obtain R_u in the range between ≈ 12 and 14% and GOF values in the range of 1.6–2.2.

Figure 4 shows a schematic structure model in side view. The interlayer spacings ($\Delta d_{ij}/d_{ij}$) relative to the bulk values^[30] are indicated on the right. In the SXR D refinement, only the topmost QL was considered, the relaxations of deeper layers were found to be insignificant. First of all, we find good agreement between the refined values derived from the ESRF and laboratory data for the pristine sample. In detail, the top inter-layer expansion $\Delta d_{12}/d_{12}$ equals to +1.8% for the ESRF and +2.7% for the laboratory experiment data (bulk: $d_{12} = 1.578 \text{ \AA}$). Furthermore, a small contraction of the second spacing is observed ($\Delta d_{23}/d_{23} = -1.7\%$, LAB: -2.4%), while the deeper ones are almost unrelaxed. For $\Delta d_{34}/d_{34}$ we find a disagreement of $\approx 3\%$, corresponding to 0.07 Å between the ESRF and laboratory data which we set as an upper limit for the uncertainty of $\Delta d_{ij}/d_{ij}$. Finally, with regard to the structural disorder we find Debye-parameters in the range of $B = 2\text{--}5 \text{ \AA}^2$, which is enhanced as compared to typical values in bulk structures ($B_{\text{bulk}} = 0.5\text{--}1.5 \text{ \AA}^2$, see Table 1).

The expansion of the top layer spacing (d_{12}) in the case of the pristine sample comes as a surprise, since for uncovered surfaces d_{12} is known to be contracted in general. An expansion in this as well as in other cases (e.g., Pd(001)^[45]) might be attributed to surface adsorption or intercalation of a foreign species into subsurface interstitial sites, such as the octahedral site between the topmost selenium and the second bismuth layer (see Figure 4). In situ dosing the sample with molecular hydrogen as well as with noble gases while simultaneously collecting SXR D data did not indicate any notable effect, leaving the presence of carbon as one remaining source of the expansion. In order to investigate this possibility, we have dosed the surface by 8.4×10^4 Langmuir (L, $1 \text{ L} = 10^{-6} \text{ Torr s}^{-1}$) of C_4H_6 under simultaneous irradiation with electrons ($E_{\text{kin}} = 500 \text{ eV}$) emitted from a flood gun (sample current $\approx 600 \mu\text{A}$). This lead to the appearance of a C-KLL Auger-transition.^[15] The

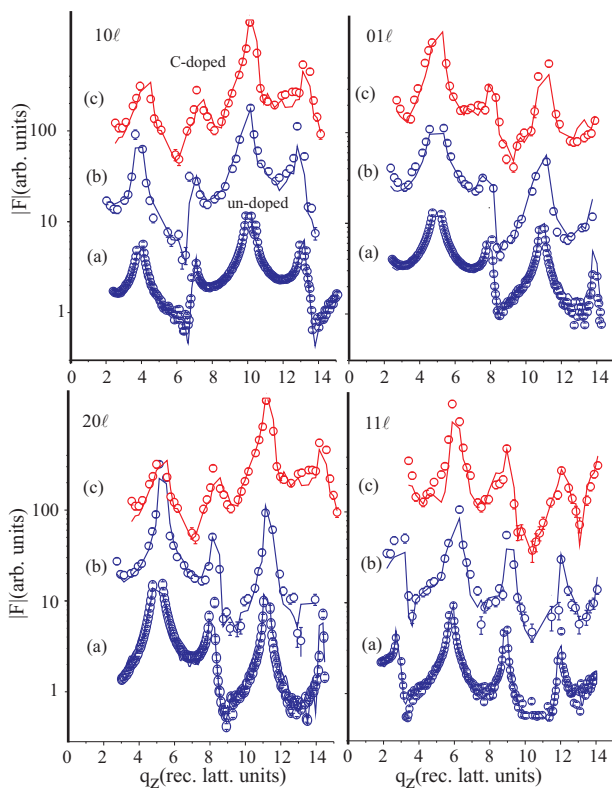


Figure 5. Fit of calculated (lines) to experimental (symbols) structure factor amplitudes $|F(hk\ell)|$ collected for a pristine (blue) $\text{Bi}_2\text{Se}_3(0001)$ and a carbon-doped (red) single crystal. Data for the pristine surface were collected at the ESRF (a) and in the laboratory (LAB) (b). Those for the carbon-doped $\text{Bi}_2\text{Se}_3(0001)$ in the laboratory only (c). Curves are shifted for clarity. Reprinted figure with permission from ref. [15]. Copyright (2014) by the American Physical Society.

subsequent SXRD analysis confirms that the top layer expansion is related to carbon interstitials.

The upper curves (red) labeled by (c) in Figure 5 represent the $|F(hk\ell)|$ of the carbon-doped sample collected in the laboratory experiment. Direct inspection of the CTRs in Figure 5 shows significant differences as compared to those of the pristine sample especially near the anti-phase positions. The corresponding structure parameters derived from the fit are listed on the right of Figure 4. There is a pronounced expansion of almost $\Delta d_{12} = 11\%$, while the other interlayer spacings remain unrelaxed within the experimental uncertainty of $\pm 3\%$.

In summary, the structure analysis of the pristine $\text{Bi}_2\text{Se}_3(0001)$ surface has provided evidence that carbon atoms present in subsurface interstitial sites induces an expansion of the top layer spacing. Ab initio calculations support this result. The interstitial site between the first and second layer is at least 0.69 eV more favorable than any other site (e.g., high-symmetry surface adsorption sites like top, bridge, fcc-, and hcp-hollow). The modification of the surface structure by the presence of interstitial carbon is also expected to modify the TSS. Previous studies have reported the modification of the TSS as well as the appearance of new states resulting from surface adsorption.^[46–52] In the following, the effect of carbon lattice expansion on the TSS is discussed on the basis of spin-resolved photoemission experiments.

4.2. Electronic Structure of the Pristine $\text{Bi}_2\text{Se}_3(0001)$ Surface

Photoemission spectroscopy measurements of the pristine Bi_2Se_3 surface were carried out using the momentum microscope. Figure 6(a) shows a constant energy image recorded at the Fermi energy (E_F). Photoemission data were integrated for a total of 200 s using unpolarized He-I radiation from a gas discharge

lamp as excitation source, incident along the $\bar{K} - \bar{\Gamma} - \bar{K}$ direction. As outlined above, the x- and y-coordinates in Figure 6 (a) directly correspond to the parallel crystal momentum coordinates, as recorded by the CCD camera of the momentum microscope. The accessible k-space region in the experiment is only determined by the photoemission horizon^[22] given by the photon energy ($h\nu = 21.22$ eV) and the work function of the sample surface ($\Phi_{\text{Bi}_2\text{Se}_3} = 5.61$ eV). At the Fermi energy, this results in a radius of this “momentum disc” of 2.02 \AA^{-1} for pristine Bi_2Se_3 .

The momentum disc in Figure 6(a) comprises the full first surface Brillouin zone (SBZ), and additionally the surrounding adjacent second SBZs, centered around the respective $\bar{\Gamma}$ points. At the Fermi energy, pronounced photoemission intensity is only found around the $\bar{\Gamma}$ points. Note that the weak background intensity does not originate from states at E_F , but from states at $E_F - 1.86$ eV excited by the He-I β discharge line. At the $\bar{\Gamma}$ points, we observe photoemission intensity from the bulk conduction band (BCB) of Bi_2Se_3 , surrounded by the circular Fermi surface contour of the Dirac surface state. The intensity at the outer six $\bar{\Gamma}$ points is inequivalent due to different M_{if} photoemission matrix elements together with the threefold crystal symmetry.

Figure 6(b) shows the band dispersion of pristine Bi_2Se_3 along the $\bar{M} - \bar{\Gamma} - \bar{M}$ direction, including the second SBZ $\bar{\Gamma}$ points. The D_p is located at about 300–400 meV below E_F . This is usually observed for naturally grown Bi_2Se_3 , where the Fermi level is fixed due to intrinsic *n*-doping by selenium vacancies and which crosses the BCB. Below $E_F - 1$ eV strong intensity from the bulk valence bands (BVB) abruptly sets in.

Figure 7(a) shows a detail of the TSS of the *pristine* Bi_2Se_3 sample. The figure shows a section along the $\bar{K} - \bar{\Gamma} - \bar{M}$ direction, extracted from the full 3D band dispersion experimentally derived using the momentum microscope. Binding energies are given relative to E_F . For this particular sample, the

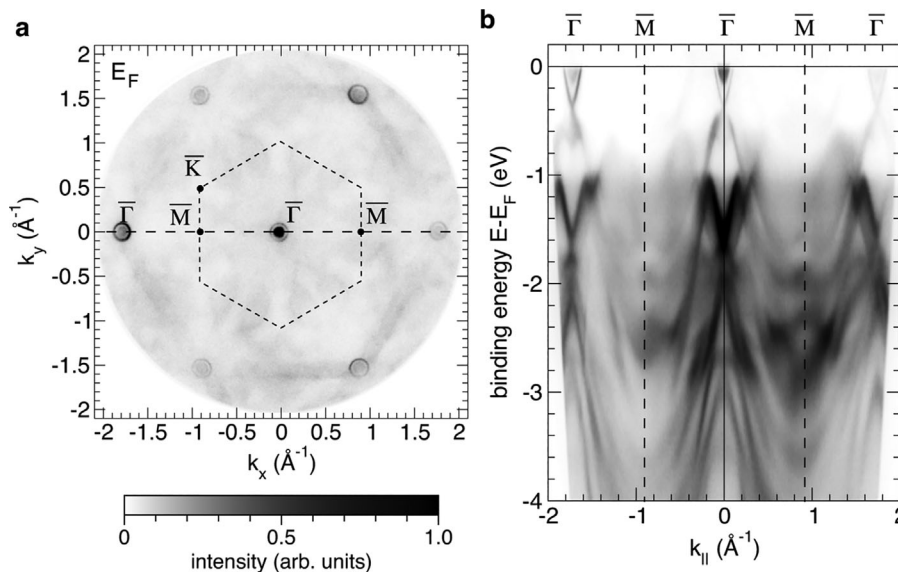


Figure 6. Momentum-resolved photoemission measurement of the pristine Bi_2Se_3 surface illuminated with unpolarized He-I radiation. a) 2D momentum disc showing the Fermi surface contour including the full first surface Brillouin zone (dashed hexagon) and surrounding second Brillouin zones. b) Band dispersion of pristine Bi_2Se_3 along the $\bar{M} - \bar{\Gamma} - \bar{M}$ direction. Binding energies are given relative to the Fermi level (E_F).

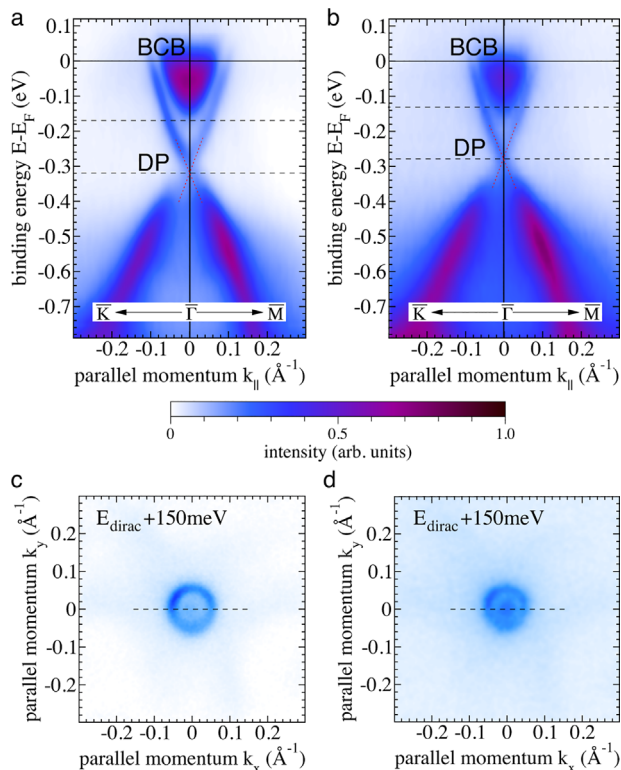


Figure 7. Momentum-resolved photoemission measurement: band dispersion of the pristine (a) and carbon-doped (b) Bi_2Se_3 along the $\bar{K} - \bar{\Gamma}$ and $\bar{\Gamma} - \bar{M}$ direction. Dotted straight lines serve as a guide to the eye to the band dispersion in the vicinity of the D_P . Binding energies are given relative to the Fermi level (E_F). Horizontal lines indicate the energy level of the D_P and the k_{\parallel} contour for the pristine (c) and doped (d) samples. Reprinted figure with permission from ref. [15]. Copyright (2014) by the American Physical Society.

experiment finds the energy position of the D_P at $E_F - 320$ meV, in agreement with results in Figure 6(b). Intensities above E_F are related to the fractional filling of bands due to the width of the Fermi-Dirac distribution. Dotted straight lines serve as a guide to the eye to the band dispersion in the vicinity of the D_P . Below the D_P , the surface state bands show a deviation from a “massless” linear dispersion, but have a slight parabolic curvature, i.e., a finite effective mass.

To investigate the effect of a modification of the surface geometric structure, like the vertical interlayer expansion of the topmost Se–Bi distance discussed in Section 4.1, we have carried out additional momentum microscope measurements of the electronic structure of *doped* Bi_2Se_3 samples. As outlined above, the reason for an up to almost 11% increased top interlayer spacing is the presence of interstitial carbon atoms (see Figure 4). In the experiments, carbon doping in the top layer region was carried out by exposing the sample to C_4H_6 , resulting in an increased layer spacing as shown in the right column in Figure 4.^[15,16]

In the photoemission experiment, carbon doping leads to an energetic upward shift of the D_P relative to E_F by 40 ± 20 meV, as shown in Figure 7(b). Dotted lines at the D_P in Figure 7(b), indicate a better agreement with a linear dispersion. The trend

toward a more linear band dispersion at the Dirac point with increasing carbon doping is confirmed by calculated band structures with expanded interlayer distances.^[15]

Most importantly, the energetic distance between the parabolic BCB, that extends from the Fermi level into the upper Dirac cone, gets reduced upon carbon doping. This is best observed in the constant energy contour of the Dirac cone, displayed at an energy of 150 meV above the D_P in Figure 7(c and d) for the pristine and doped sample, respectively. At this energy the conduction band minimum for the pristine sample does not appear in the momentum image, and we observe an un-filled circular contour of the TSS in Figure 7(c). By contrast, significant additional intensity from the conduction band is present in Figure 7(d) for the carbon-doped sample. Note that both images were monitored at the same energy above the D_P , respectively.

Expansion of the topmost Se–Bi interlayer distance preserves the TSS at the Bi_2Se_3 surface. The surface state, however, is modified in two ways: i) the binding energy of the D_P is shifted upwards *relative to the BCB*. This leads to a filling of the inner region of the upper Dirac cone by bulk states. With increasing layer expansion, it therefore becomes increasingly difficult to separate the TSS from bulk states in the experiment. ii) The dispersion of the Dirac surface state, being not linear below the D_P for pristine surfaces, becomes more linear with increasing interlayer expansion.

The outstanding properties of the TSS which is formed at the interface between a three-dimensional TI like Bi_2Se_3 and the vacuum manifest in an unconventional spin-momentum locking of the respective electron states. The spin of an electron is locked perpendicular to its crystal momentum thus being protected from the elastic backscattering, a property provided by time-reversal symmetry. It is this property that makes the topological surface state robust against a class of perturbations which respects time-reversal symmetry.^[53–55]

To measure the spin texture of the topological surfaces state therefore received major attention in photoemission studies. The experimental resolution in terms of energy ΔE and parallel momentum (Δk_{\parallel}) that is required to probe the TSS poses a fundamental challenge for such studies. A major limitation in most spin-resolved photoemission experiments is the notorious inefficiency of electron spin detection, which was only recently overcome by novel multi-channel spin analyzers.^[56] Nevertheless, first spin-resolved photoemission experiments seemed to confirm the expected spin momentum locking of the surface state.^[57,58] However, later experiments showed that this picture might be more intricate, as the measured photoelectron spin depends on the optical polarization of the exiting light.^[59–64] These results suggested that the apparent spin texture probed in the photoemission experiment might reverse between photoemission using s- and p-polarized light and the spin direction might become even out-of-plane for circular-polarized light.

The dependence of the spin polarization of photoelectrons emitted by linear-polarized light is displayed in our spin-resolved measurements of the TSS on Bi_2Se_3 in **Figure 8**. For both polarizations, the light is incident along the k_x axis. As indicated in Figure 8(a) and (b), the electric field vector (\mathbf{E}) is parallel to the y-axis for s-polarization and within the optical plane for p-polarization. Using s-polarization in Figure 8(a), the spin-resolved momentum map at the Fermi energy shows the

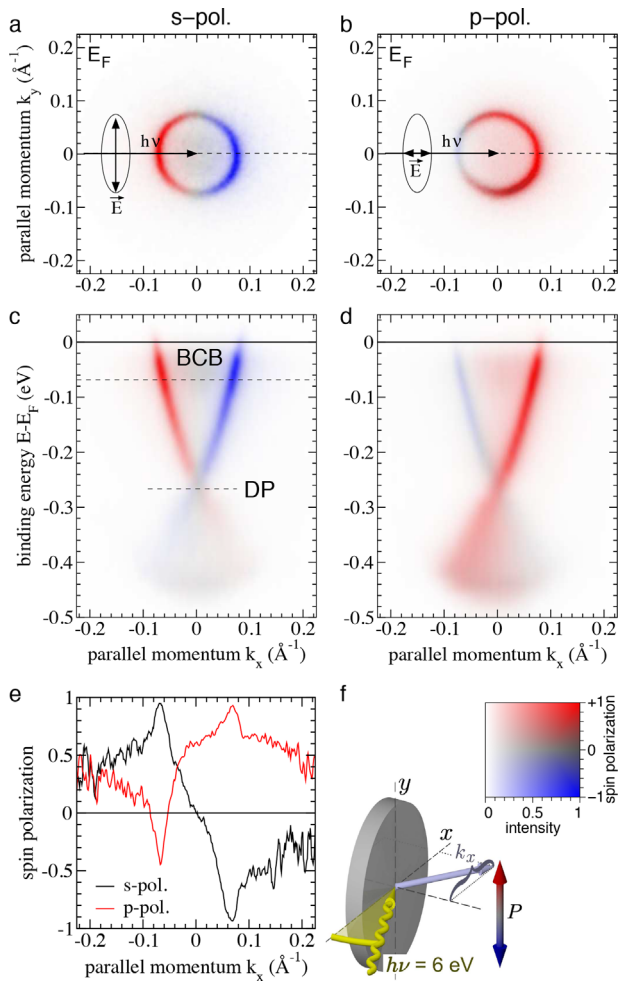


Figure 8. Spin-resolved measurement of the TSS of pristine Bi_2Se_3 excited by linear polarized 6.0 eV laser radiation. Spin-resolved photoemission intensity for s-polarized (a and c) and for p-polarized light (b and d). Red, blue, and gray shading corresponds to photoelectron spin polarization along the k_y in-plane direction and intensities according to the two-dimensional color code and photoemission geometry displayed in (f). e) Horizontal profile of the measured spin polarization for s- and p-polarized light at E_F .

characteristic spin-momentum locking of the TSS with directly opposite P_y -spin-polarization (red and blue colors) for positive and negative k_x . In the energy dispersion of the surface state along the k_x -axis (Figure 8c), this is as well reflected as two bands of opposite polarization crossing at the D_p . The polarization in the surface state bands reaches values of up to $\pm 95\%$, while the BCB is not significantly spin-polarized. For p-polarized light, displayed in Figure 8(d), the spin polarization of the surface state bands is reversed, in agreement with previous studies. Note that there is an additional asymmetry of intensities between the left and right half of the dispersion, observed for p-polarized light. This is due the off-normal incidence of the light, and known as the linear dichroism of the angular distribution (LDAD).^[65–67]

The LDAD effect observed in the photoemission intensities is also reflected in the measured spin-polarization. The spin-polarization at E_F along the horizontal profile, displayed in

Figure 8(e), shows a pronounced asymmetry between positive and negative k_x for p-polarization. In this case, also non-zero spin-polarization of the BCB states is observed. Such an asymmetry in the photoelectron spin-polarization can be related to a different LDAD of spin-up and spin-down electron states, being locked to different orbital contributions. It was recently shown that in such case the observed spin texture might even reverse as a function of photon energy by probing different contributions of the electron wave functions.^[68] The observation of the LDAD together with the spin-polarization therefore provides a strong tool to map the full spin-orbital texture of electron states with strong spin-orbit coupling.

The observation of spin-polarized photoelectrons depending on the incident light polarization is not a new effect, in general. For photoemission from metal surfaces a spin-polarization depending on the incident light polarization was already observed even for a non-polarized ground state, and termed “optical spin orientation.”^[69] For TIs, in particular Bi_2Se_3 , a similar mechanism leads to selective photoemission from different ground state orbital components of the initial state wave functions,^[64] and is not related to a “spin-flip” happening in the photoemission process, as proposed earlier.^[61] The concept that different orbitals are locked to a different spin component is a direct consequence of the large spin-orbit coupling present in TIs. The observation of opposite photoelectron spin-polarizations surface states of related—but topological trivial—materials such as BiTeI reveals that this effect is not due to topological protection, but large spin-orbit coupling.^[70]

5. Preparation of a Bismuth Bi-Layer on $\text{Bi}_2\text{Se}_3(0001)$ by Selective Hydrogen Etching

5.1. Geometric Structure

While Bi_2Se_3 represents the “classic” three-dimensional (3D) TI, the first prediction of a 2D TI goes back until 1986.^[71] Surprisingly, 2D TIs have been much less investigated. 2D TIs are characterized by one-dimensional (1D) edge states which have been predicted and observed more than 10 years ago by monitoring the quantized conductance in HgTe/CdTe semiconductor quantum well structures.^[72,73] Owing to its large spin-orbit coupling, bismuth is a primary candidate for a 2D TI and bismuth bi-layers (BLs) have been intensely studied.^[74,75] To prepare bismuth BLs several “bottom-up” techniques have been employed in the past such as molecular beam epitaxy (MBE),^[76–79] exfoliation,^[80] or preparing a clean $\text{Bi}(111)$ surface and investigating step edges.^[81] We have used a novel “top-down” technique taking advantage of selective etching of selenium atoms when $\text{Bi}_2\text{Se}_3(0001)$ is exposed to a flux of atomic hydrogen^[18] generated by a microwave-driven (2.45 GHz), SPECS PCS-ECR plasma source, operated in the atom-beam mode.^[82] During operation of the atom source, the hydrogen partial pressure in the chamber was $p_{\text{H}_2} \approx 5 \times 10^{-5}$ mbar. The partial pressure was used for the quantification of the exposure expressed by Langmuir (L) units ($1 \text{ L} = 10^{-6} \text{ Torr s}^{-1}$). Prolonged dosing up to 4200 L resulted in an atomically flat bismuth BL several hundreds of nanometers wide as evidenced by STM as shown in Figure 9.

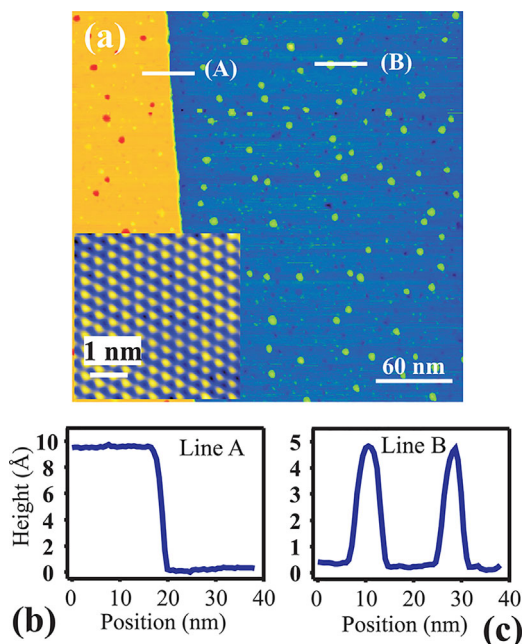


Figure 9. a) Topographic STM image ($300 \times 300 \text{ nm}^2$, $U = 1 \text{ V}$, $I = 200 \text{ pA}$) of the topmost bismuth layer of the BL film on $\text{Bi}_2\text{Se}_3(0001)$ prepared by exposing Bi_2Se_3 to 4200 L of atomic hydrogen. Two profiles along the lines “A” and “B” are shown in (b) and (c), respectively. The inset shows an atomically resolved image of the bismuth surface. Reprinted figure with permission from ref. [18]. Copyright (2015) by the American Physical Society.

The profiles shown in Figure 9(b) and (c) show approximately 9.5 Å high steps characteristic for the QL and 4.2 Å high islands with a diameter of 5 nm. In combination with the complete disappearance of the selenium Auger-transition at $\approx 43 \text{ eV}$,^[18] it is concluded that the STM image shows the surface of a bismuth bi-layer covered by small bismuth bi-layer high islands. The atomically resolved image in the inset in (a) evidences the well-ordered hexagonal arrangement of the top layer bismuth atoms. The direct proof for the STM-based structural model is provided by SXR D.

Symbols in **Figure 10** represent the experimental structure factor amplitudes ($|F_{\text{obs}}(hk\ell)|$) along several CTRs collected for the $\text{Bi}_2\text{Se}_3(0001)$ sample after hydrogen exposure. Integrated intensities $I_{\text{tot}}(hk\ell)$ with $|F_{\text{obs}}(hk\ell)| \propto \sqrt{I(hk\ell)}$ were collected by a 2D pixel detector and corrected for instrumental factors^[37,38] As outlined above, the analysis of the adsorbate structure is based on the interference between the scattering amplitude of the semi-infinite substrate formally expressed by the structure factor $F_{\text{CTR}}(hk\ell)$ and that of the adsorbate, $F_{\text{ad}}(hk\ell)$, given by $I_{\text{tot}}(hk\ell) \propto |F_{\text{CTR}}(hk\ell) + F_{\text{ad}}(hk\ell) \times \exp[i\phi]|^2$, where the phase factor accounts for the registry of the adsorbate structure relative to the substrate.

The structure analysis was carried out by fitting calculated structure factor amplitudes ($|F_{\text{calc}}|$) to the $|F_{\text{obs}}(hk\ell)|$ ones. As in the case of the pristine $\text{Bi}_2\text{Se}_3(0001)$ sample, the high $p3m1$ plane group symmetry facilitates the analysis, since all atoms reside on a threefold rotation axis allowing only the positional parameter z to vary. In addition, one overall Debye parameter $B = 8\pi(u^2)$ was

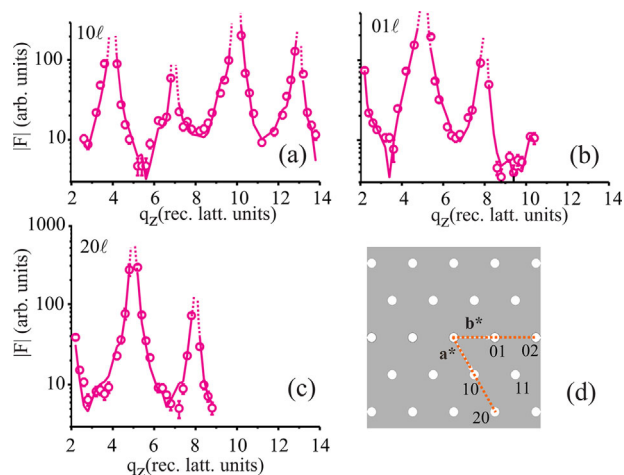


Figure 10. a–c) Experimental (symbols) and calculated (lines) structure factor amplitudes $|F_{\text{tot}}|$ along crystal truncation rods of Bi_2Se_3 after exposure to atomic hydrogen. Fit corresponds to structure model shown in Figure 11. d) Schematic of the reciprocal space in the $a^* - b^*$ plane. Reprinted figure with permission from ref. [18]. Copyright (2015) by the American Physical Society.

refined. Based on the structure model schematically sketched in **Figure 11**, a good fit ($R_u = 0.12$) could be achieved which is represented by the solid lines in Figure 10.

As schematically shown in Figure 11, a bismuth BL covers about 80–90% of the surface on a $\text{Bi}_2\text{Se}_3(0001)$ crystal which is terminated by selenium. The SXR D analysis also finds a 5–10% fraction of double layer vacancies and BL high ($\approx 4 \text{ \AA}$) bismuth islands, in close agreement with the STM image. In conclusion, surface treatment with atomic hydrogen has completely removed selenium which – in a simple way – might be described by: $\text{Se} + 2\text{H} \rightarrow \text{H}_2\text{Se} \uparrow$. Only two bismuth layers of the QL are left behind. This bismuth BL serves as a protective layer, because it is etched by significantly lower rate than selenium facilitating the preparation of the bismuth BL since no accurate calibration of the hydrogen dosage is required.

The SXR D analysis also allows the detailed analysis of the interlayer relaxations and interatomic distances. Along the bulk bismuth [0001] direction a long (2.35 Å) and a short (1.59 Å) distance alternate corresponding to the strength of the inter layer bonds which are of vdW and covalent type, respectively.^[83,84] As compared to the bulk value of 1.59 Å the vertical spacing of 1.78 Å within the BL ($\text{Bi}_3\text{-Bi}_4$) corresponds to an expansion of $\approx 12\%$. This is related by elasticity to the -8.8% compression of the bismuth BL in registry with $\text{Bi}_2\text{Se}_3(0001)$ (lattice parameter $a_0 = b_0 = 4.14 \text{ \AA}$ on Bi_2Se_3 vs. 4.54 Å for bulk bismuth). For more details, we refer to ref. [18]. Notably, there is a large 2.29 Å vertical spacing between the lower bismuth layer (Bi_4) and the topmost selenium layer (Se_1) of the $\text{Bi}_2\text{Se}_3(0001)$ surface in perfect agreement with theory. The results of DFT calculations are listed by the numbers in brackets in Figure 11. This suggests that the interaction between the bismuth film and the substrate is weak, which might be important for the stabilization of the 2D topological character of the bismuth BL. In general, it can be summarized that – apart from relaxations induced by lateral strain due to epitaxial growth – the structure of the bismuth film

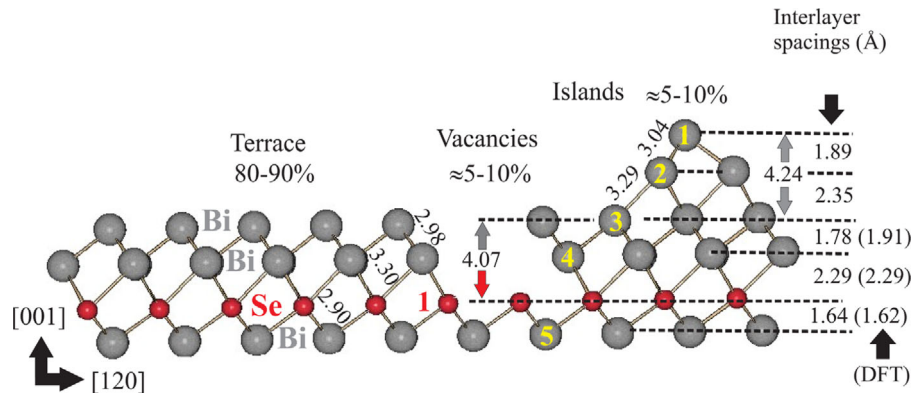


Figure 11. Side view of the near surface region of atomic hydrogen exposed Bi_2Se_3 . Large gray and small red spheres correspond to bismuth and selenium atoms, respectively. Numbers represent distances in Angstrom units. Values in brackets label DFT calculated interlayer spacings. Bismuth and selenium layers are labeled by yellow and red numbers beginning with “1” from the top. Reprinted figure with permission from ref. [18]. Copyright (2015) by the American Physical Society.

resembles that of the bulk. The characteristic sequence (long/short/long/...) of the vertical spacings is present in the film and even continues into the islands (2.35 and 1.89 Å, see bismuth atoms [1,2,3]).

5.2. Electronic Structure

The SXRD experiments have proven that the hydrogen etched $\text{Bi}_2\text{Se}_3(0001)$ surface is characterized by a bismuth BL. Its electronic structure was recently investigated by ARPES.^[85] The upper panels in **Figure 12** show the ARPES (a) and its derivative (b), the latter to enhance the contrast. The spectra are characterized by two crossing points labeled by D_{TI} and D_{Bi} which are attributed to the Bi_2Se_3 derived D_{P} and to the band crossing of two Rashba-split hole-like bands, respectively. For the D_{TI} a decreased Fermi velocity ($v_{\text{F}} = 2.58 \times 10^5 \text{ m s}^{-1}$) was derived which is reported to be a factor two smaller than for the pristine surface ($v_{\text{F}} = 5.71 \times 10^5 \text{ m s}^{-1}$) and which is tentatively attributed to the interaction between the TSS and quantum well states.^[85]

Figure 12(c) and (d) show the calculated spin-resolved spectral weights along the k_x ($\bar{\Gamma} - \bar{K}$) and the k_y ($\bar{\Gamma} - \bar{M}$) direction indicating the presence of the spin-momentum locking. The Rashba coupling in this case is exceptionally high as measured by the coupling constant (a) given by $a = 2\Delta E/\Delta k$. Giant values of $a = 4.5$ and 4.0 eV \AA^{-1} are derived along k_x and k_y , respectively, which are even larger than in bulk BiTeI ($a = 3.8 \text{ eV \AA}^{-1}$).^[86] In the bismuth BL-covered Bi_2Se_3 , the charge density related to the TSS is shifted down to the second QL^[18,85] resulting from the hybridization between the BL and the substrate. This giant Rashba-type splitting makes the top-down prepared bismuth BL on Bi_2Se_3 interesting for potential applications in spintronics.

6. Gap Opening by Gold Substitution in Bismuth Sites

Adsorption of gold in the sub-monolayer range on the $\text{Bi}_2\text{Se}_3(0001)$ surface leads to the opening of a gap at the D_{P} of the TSS. This section discusses in detail the analysis of the

local geometric structure around the gold atoms using extended X-ray absorption fine structure (EXAFS) experiments above the Au-L_{III}-edge ($E_0 = 11\,919 \text{ eV}$) and its relation to the modification of the surface electronic structure as derived from spin- and momentum-resolved photoemission experiments.

6.1. Geometric Structure Analyzed by EXAFS Experiments

EXAFS is ideally suited to study the local structure around an impurity species like a dopant introduced into the surface of

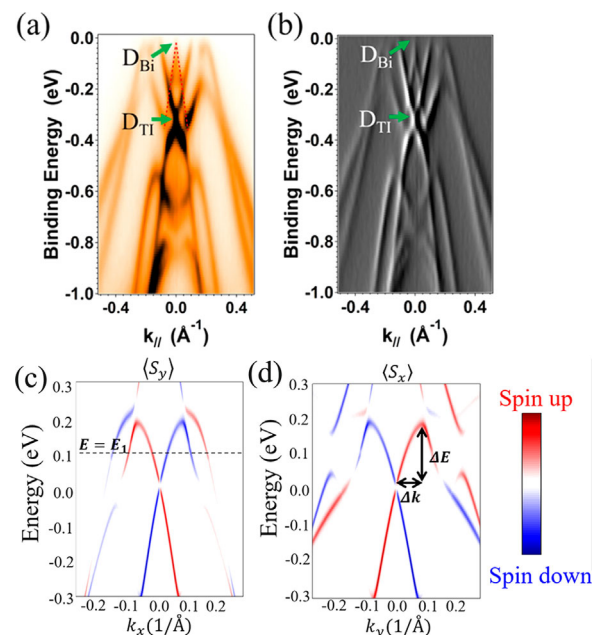


Figure 12. a) ARPES of bismuth bilayer on $\text{Bi}_2\text{Se}_3(0001)$ along the $\bar{\Gamma} - \bar{K}$ direction. b) Derivative of (a). c) and d) Calculated spectral weight of spin-polarization for the k_x ($\bar{\Gamma} - \bar{K}$) and the k_y ($\bar{\Gamma} - \bar{M}$) direction. Note that giant Rashba splitting expressed by Δk . For details see text. Reprinted figure with permission from ref. [84]. Copyright (2017) American Chemical Society.

Bi_2Se_3 . It reveals both the nearest neighbor distances as well as the (effective) number of nearest neighbors. In addition, the polarization dependence of the effective coordination number allows to separate between high (e.g., bulk cubic like environment) and low (surface) symmetry sites. In the following, the most important aspects of EXAFS are outlined as far as they are necessary for the understanding of the analysis of the Au/ $\text{Bi}_2\text{Se}_3(0001)$ adsorption system. For further reading we refer to textbooks.^[87–89]

EXAFS is the oscillatory modulation of the energy-dependent linear absorption coefficient $\mu(E)$ relative to the smoothly varying background $[\mu_0(E)]$ which is observed in the energy range several hundred electronvolt past an absorption edge at energy E_0 . **Figure 13** shows $\mu(E)$ versus photon energy in the vicinity of the Au-L_{III} absorption edge ($E_0 = 11\,919$ eV). The data were collected in the fluorescence yield (FY) mode after deposition of about 0.6 ML of gold on the $\text{Bi}_2\text{Se}_3(0001)$ surface kept at a temperature of 160 K. The experiments were carried out at the Sector 20 insertion device beamline at the Advanced Photon Source (APS), Argonne National Laboratory (USA). One ML is equal to 6.74×10^{14} atoms/cm², i.e., one ad-atom per surface atom.

The fine structure in $\mu(E)$ above an absorption edge is known since almost a century. The first observations were made in 1920 by H. Fricke^[90] and by G. Hertz^[91] and theoretically interpreted by R. de Kronig^[92] based on long range order theory. It took until the early 1970s to formulate a correct theory of EXAFS in terms of short range order.^[93] It also established a path for the analysis using the Fourier Transformation (FT) of the interference function $[\chi(k)]$ which is defined as $\chi(k) = [\mu(E) - \mu_0(E)]/\mu_0(E)$, where k represents the wave-number of the electron at an energy E above E_0 according to the relation: $k = \sqrt{2m(E - E_0)/\hbar^2}$. The interference function is shown in the inset of Figure 13 for both

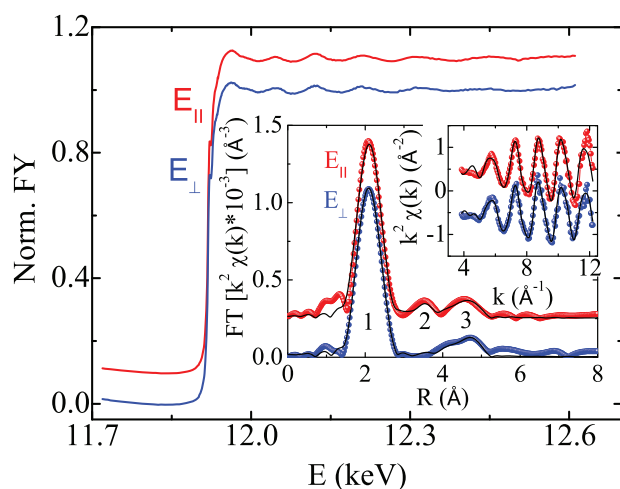


Figure 13. EXAFS spectra collected in the fluorescence yield after deposition of 0.6 ML of gold on $\text{Bi}_2\text{Se}_3(0001)$. The two curves labeled by (E_{\parallel}) and (E_{\perp}) correspond to different experimental geometries in which the electric field vector (E) is either parallel (E_{\parallel}) or perpendicular (E_{\perp}) to the sample surface. Curves are shifted for clarity. The inset in (a) shows the k^2 -weighted interference function $[\chi(k)]$ and the magnitude of the Fourier Transforms. For details see text. Reprinted with permission from ref. [111]. Copyright (2017) by the American Physical Society.

polarizations. It contains all information regarding the local structure around the absorbing atom which is expressed by the formula:

$$\chi(k) = \sum_i \frac{S_0^2 N_i^* F_i(k)}{k R_i^2} e^{(-2k^2 \sigma_i^2)} e^{(-2R_i/\lambda_i)} \sin[2kR_i + \delta_i(k)] \quad (6)$$

with backscattering amplitude $F_i(k)$, mean-free-path (λ_i), and phase shift $[\delta_i(k)]$ of the i -th shell. The parameter S_0^2 describes the effect of the relaxation of the $(N - 1)$ “passive” electrons on the EXAFS amplitude after the photoelectron is emitted.^[89,94] The remaining parameters, N_i^* (effective coordination number), R_i (distance), and σ_i^2 (mean-square-relative-displacement) are available to be fit. Of special interest is the parameter N_i^* which in the case of K-shell EXAFS (angular momentum $\ell = 0$) depends on the angle (α_{ij}) between the electric field vector (\vec{E}) and the interatomic vector \mathbf{R} between absorber and backscattering atom according to:

$$N_i^* = 3 \sum_{j=1}^N \cos^2(\alpha_{ij}) \quad (7)$$

where the summation extends over all neighboring atoms j of the i -th shell. Absorption from an $L_{2,3}$ edge (angular momentum $\ell = 1$) has a more complicated polarization dependence given by:

$$N_i^* = (0.5 + c) \times N_i + (1.5 - 3 \times c) \times \sum_{j=1}^N \cos^2(\alpha_{ij}) \quad (8)$$

with $c = M_{01}/M_{21} \approx 0.2$ being the ratio of the radial dipole matrix elements for the transition from the p-initial state ($\ell = 1$) to the s ($\ell = 0$) and to the d ($\ell = 2$) final state, respectively. As discussed by Citrin^[95] in detail, the above equation is valid in the case that no phase shift exists between the outgoing s- and d-wave. Most importantly, in the case of a cubic or isotropic environment the relation $N_i^* = N_i$ holds for both K and L-edge EXAFS, i.e., the effective coordination number is equal to the “real” one. The analysis is carried out by calculating the FT of the k^n weighted function $\chi(k)$ according to:

$$\text{FT}(R) = \int_{k_{\min}}^{k_{\max}} \chi(k) \times k^n \times e^{i2kR} dk \quad (9)$$

using proper integration limits k_{\min} and k_{\max} at zero crossings of $\chi(k)$. Here we have chosen $k_{\min} = 3.78$, $k_{\max} = 12.05$, and $n = 2$. The FT magnitude in Figure 13 shows three peaks labeled by 1–3 for E_{\parallel} , but only 1 and 3 for E_{\perp} . Peak 1 corresponds to two nearby selenium shells (see below), while peaks 2 and 3 are related to higher shells. For the present discussion we focus on the first peak only, which was fitted in R-space within the range between $R = 1.56$ and 2.71 \AA filtered by multiplying $\text{FT}(R)$ with a Gaussian window. The analysis was carried out by using the program WinXAS.^[96] Fits are shown as solid lines in Figure 13 superimposed on the experimental data. Very similar to the SXRD case, the fit quality is given by the un-weighted residuum

(R_u) which measures the average relative deviation between the observed (Y_{obs}) and the calculated (Y_{calc}) magnitudes of FT(R) within the selected window.^[97]

Direct inspection of the FTs indicates that there is no polarization dependence of the EXAFS amplitude, i.e., to within about 10% the condition $N_{\perp}^* = N_{\parallel}^*$ holds, thus suggesting that gold resides in a cubic-like environment. In **Table 2**, the parameters characterizing the local gold environment are listed for E_{\parallel} and E_{\perp} which were obtained by two different approaches. For E_{\parallel} , we have kept fixed N_1^* and N_2^* to the values calculated on the basis of Equation (8) for the substitutional site and a complete coordination shell ($N_1^* = 3.03$, $N_2^* = 2.92$). This site is compatible with the isotropy of the EXAFS amplitude and the fitted distances of $R_{\text{Se}1} = 2.45(3)$ and $R_{\text{Se}2} = 2.65(4)$ Å. Comparison with the distances in unrelaxed bulk Bi_2Se_3 (2.87 and 3.07 Å) indicates considerable relaxation of the local structure upon incorporation into the substitutional site. For this approach we find a good fit as given by $R_u = 4.9\%$. However, while this result provides evidence for gold to be located in the substitutional site, one can go one step further by allowing the effective coordination numbers N_1^* and N_2^* to be different from the values for complete coordination and by simultaneously allowing the distances R_1 , R_2 , mean squared relative displacements (MSRD) (σ_1^2 , σ_2^2) and the energy shift $\Delta E_1 = \Delta E_2$ for both shells (subscripts 1,2) to vary. The results are listed for the E_{\perp} data in Table 2.

Allowing for a variation in N_1^* and N_2^* improves the fit to values in the range between $R_u = 0.6$ and 0.8. The best fit is obtained for $N_2^* = 1.5$, but a similar quality can also be achieved with $N_2^* = 2.5$ –3.0, thus adding to a total effective coordination in the range of $N_{\text{tot}}^* = 3.5$ –5.0. Distances were found to be $R_1 = 2.44$ Å and $R_2 = 2.65$ Å with an error bar of $\Delta R_1 = 0.03$ Å and $\Delta R_2 = 0.10$ Å for the first and second shell, respectively (see Table 2). The presence of two nearby selenium shells around a substitutional gold atom comes not unexpected: we recall that in the bulk Bi_2Se_3 structure, bismuth atoms in the second and fourth layers of each QL reside in an asymmetric environment with three selenium atoms (first and fifth layers) being closer ($R = 2.87$ Å) than the three selenium atoms in the third layer ($R = 3.07$ Å). Thus one may expect that this asymmetry is also experienced by the gold atoms in this site, even after some

Table 2. Structure parameters for 0.6 ML Au gold on Bi_2Se_3 . The meaning of the parameters is as follows: R , refined neighbor distance; R_b , distance in unrelaxed bulk structure; N_b , coordination in the bulk structure; N^* , effective polarization-dependent coordination number for L_{III} edge^[95]; σ^2 , mean squared relative displacement amplitude; ΔE_0 , shift of absorption edge; R_u , residual in percent.^[97] The amplitude reduction factor (S_0^2) was kept constant at $S_0^2 = 0.80$ in all cases. Parameters labeled by an asterisk (*) in brackets are kept fixed. Uncertainties are given in brackets. Data reproduced from ref. [111].

Pol.	Shell	R_b (Å)	N_b	R (Å)	N^*	σ^2 (Å ²)	ΔE_0 (eV)	R_u
E_{\parallel}	Se1	2.87	3	2.45 (3)	3.04 (*)	0.004	2.6	4.9
	Se2	3.07	3	2.65 (4)	2.92 (*)	0.014	2.6	
E_{\perp}	Se1	2.87	3	2.44 (3)	2.2 (3)	0.003	−1.3	0.7
	Se2	3.07	3	2.65 (10)	1.5 (7)	0.015	−1.3	

structural relaxation. As compared to the ideal coordination with in total six selenium atoms, our EXAFS analysis indicates an incomplete coordination shell with N_{tot}^* in the 3.5 to 5.0 regime. A reduced coordination in an as grown ultra-thin film structure is quite common and is related to structural defects or the finite size of the nanostructure.

6.2. Gap Opening by Gold in Substitutional Site

In the following we outline photoemission experiments, carried out using spin-resolving momentum microscopy which provide evidence that deposition of non-magnetic gold into the substitutional sites induces an opening of a gap in the TSS. At first this appears to come as a surprise since for a long time it has been generally believed that in order to gap out the D_p an effective mass term has to be taken into account, e.g., by applying a magnetic field along the z-direction^[13,98–102] and that the D_p and the TSS were found to be robust upon deposition of various adsorbates^[15,47,103,104] and overlayers.^[18,105,106]

The first hint that the opening of a gap is not only related to ferromagnetic order was given in the study of the bulk $(\text{Bi}_{1-x}\text{Mn}_x)_2\text{Se}_3$ alloy where a large, approximately 100 meV large gap was attributed to in-gap resonance states of d-symmetry rather than to the presence of ferromagnetic order.^[107] Previous studies already suggested that impurity (vacancy) resonance states near the D_p exist^[108–110] in the bulk or in the near surface regime which hybridize with the TSS. As a consequence it is destroyed and the D_p is energetically split. In this context, it is important to note that Black-Schaffer and Balatsky^[110] pointed out that the TSS is only protected against two-dimensional backscattering, but that there is no protection against scattering processes, which involve bulk states independent on whether they originate from non-magnetic or magnetic impurities.

In **Figure 14(a–c)** we show spin-resolved spectra for 0.3, 0.5, and 1 ML Au/ Bi_2Se_3 . For 0.3 ML Au coverage, spin-resolved intensities reproduce the Dirac cone of the TSS, as observed for the uncovered surface in **Figure 8(c)**. The energy position of the D_p at about 280 meV below E_F is in good agreement with the observation for pristine Bi_2Se_3 . Note that some scatter of a few 10–100 meV of the absolute D_p energy is possible between *different samples* due to the different concentration of intrinsic doping. Compared to the pristine surface, states in the photoemission experiment appear broadened with increasing Au coverage. This is due to the increased amount of diffuse scattering, i.e., photoelectrons from the TSS are randomly scattered by Au atoms. Notably, the spin polarization is conserved, thus giving a sensitive trace of the presence of the spin-polarized TSS.

Several observations support the conclusion of the opening of a gap in the TSS with increasing Au dose. In general, the characteristic spin momentum locking of the surface state is preserved upon gold deposition for all Au coverages. However, the dispersion is not observed to continue into the energy range below the black-dashed lines in **Figure 14(b and c)** where the two spin-polarized branches meet at $k_x = 0$. In this energy range, also the spin polarization vanishes. Furthermore, the dispersion of the spin-polarized surface state is energetically compressed

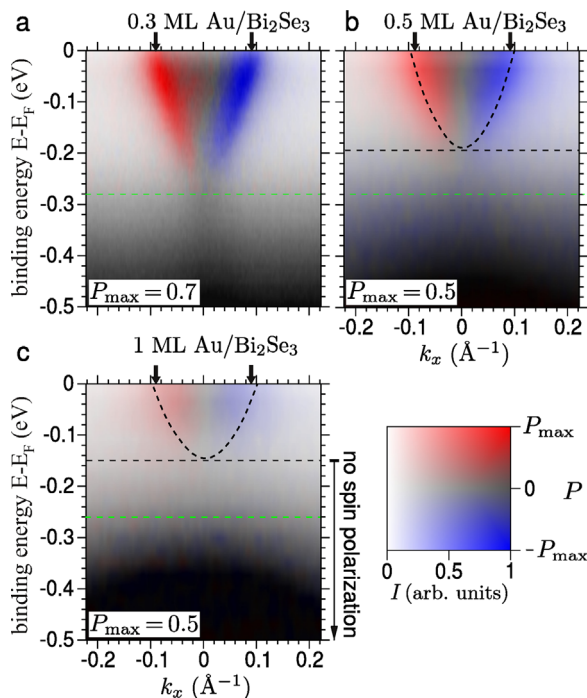


Figure 14. Spin-resolved photoemission of 0.3 (a), 0.6 (b), and 1.0 (c) ML gold-covered Bi_2Se_3 using s-polarized laser light ($h\nu = 6.0$ eV); deposition was carried out at $T = 223$ K, followed by annealing to $T = 243$ K for 5 min. Dashed lines indicate the opening of a gap in the dispersion of the surface state. Reprinted figure with permission from ref. [111]. Copyright (2017) by the American Physical Society.

instead of being shifted. The small black arrows in Figure 14(a–c) indicate that the k_x -diameter at E_F is not varying as it would result from a rigid upwards shift of the TSS.

The opening of a gap in the TSS can be understood by Au–Se bond formation, i.e., by the hybridization of the Au-d states with the Se-p states. Ab initio calculations^[111] were carried out based on the structure model derived from the EXAFS analysis for an $(\text{Bi}_{1-x}\text{Au}_x)_2\text{Se}_3$ alloy which has a concentration of $x = 0.0125$. The gold atoms are considered to occupy the bismuth substitutional sites homogeneously in both layers within the first QL. **Figure 15** shows the density of states where the blue

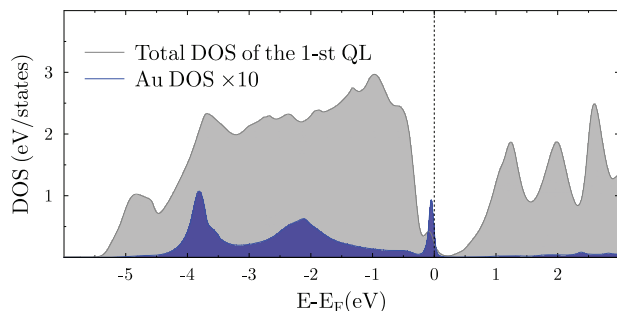


Figure 15. Density of states of the first QL in $\text{Bi}_{1.975}\text{Au}_{0.025}\text{Se}_3/\text{Bi}_2\text{Se}_3(0001)$. The blue area shows the DOS of gold scaled by factor 10. Reprinted with permission from ref. [111]. Copyright (2017) by the American Physical Society.

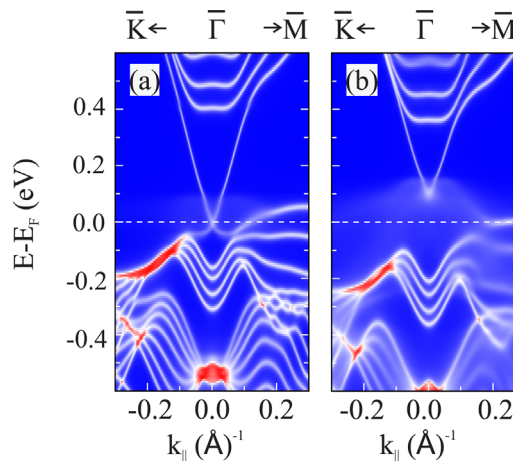


Figure 16. Calculated spectral density for $(\text{Bi}_{1-x}\text{Au}_x)_2\text{Se}_3$ alloy with $x = 0.0125$ (a) and $x = 0.125$ (b), respectively. While for $x = 0.0125$ the TSS is still ungapped, a gap of ≈ 200 meV is present at $x = 0.125$. Reprinted figure with permission from ref. [111]. Copyright (2017) by the American Physical Society.

(dark) partial DOS represents the contribution of gold to the total DOS (bright). A resonance state exists near E_F which is of d-symmetry. It is present for all concentrations (x) within the range ($0 < x \leq 0.5$). In the photoemission experiment, this Au-d resonance state is observed as the weak diffuse background intensity at the former place of the D_p . While the total DOS as shown in Figure 15 is finite around the D_p , the Au-d resonance contributes only incoherently to the spectral density, while the gap is opened in the coherent TSS due to hybridization.

The band structure of the $(\text{Bi}_{1-x}\text{Au}_x)_2\text{Se}_3$ alloy for $x = 0.0125$ (a) and $x = 0.125$ (b) is shown in **Figure 16**. The calculations were carried out using a self-consistent full relativistic Green function method especially designed for semi-infinite materials such as surfaces and interfaces.^[112] Alloying the bismuth layers with gold was simulated within a coherent potential approximation as implemented within the multiple scattering theory.^[113,114] Low, medium, and high spectral density is represented by blue, white, and red color coding, respectively. For $x = 0.0125$ the spectral density resembles that of pristine $\text{Bi}_2\text{Se}_3(0001)$ surface while even at a concentration of $x = 0.125$ a gap of $\Delta E = 200$ meV is present, in good agreement with the photoemission spectra. As observed in the photoemission experiment, the spectral density is considerably weakened in the gap region due to the presence of a resonance state and because of band broadening induced by structural disorder. Furthermore, gold acts as a p-dopant shifting the bands up in energy.

7. Summary

In summary, this review has discussed the intimate relation between subtle structural modifications and corresponding modifications of the electronic structure in pristine and adsorbate-covered $\text{Bi}_2\text{Se}_3(0001)$. This was done by combining state-of-the-art experimental tools to analyze the atomic and electronic structure with ab initio calculations. We have used SXRD which provides detailed information on the long range ordered structure,

while EXAFS as a complementary tool is sensitive to the short range order around an specific atomic species. STM – on the other hand – directly probes the surface morphology in R-space. We have applied these techniques to different samples, namely the pristine surface as well as on Bi₂Se₃ which was dosed by atomic hydrogen and gold. In all cases we find – on first view – surprising results with characteristic modifications of the surface structure: i) while for pristine Bi₂Se₃(0001) the presence of small amounts of interstitial carbon is detected related to an expansion of the top inter-layer spacing; ii) hydrogen dosing induces a complete restructuring of the near surface regime by removing all selenium from the first QL leaving a well-ordered bismuth BL behind; iii) finally, deposited gold atoms replace bismuth within the first QL. These modifications of the surface have a strong influence of the band structure as evidenced by photoemission spectra collected by the “momentum microscope.” This spans from an energetic shift of the TSS and the D_p for case (i) via the appearance of spin-polarized Rashba split hole-like states in addition to the TSS for case (ii) to the opening of a gap resulting from the presence of gold-derived d-states at E_F in case (iii). Ab initio calculations on the basis of the atomic structure have confirmed the conclusions relating atomic and electronic structure and have proven the importance of a combined investigation employing a number of complementary techniques to study TIs.

Acknowledgments

This work is supported by the Deutsche Forschungsgemeinschaft (DFG) through priority program SPP 1666. The authors thank Arthur Ernst, Andrey Polyakov, Katayoon Mohseni, Ingrid Mertig, Dirk Sander, Sumalay Roy, Roozbeh Shokri, Evgenii Chulkov, Mikhail Otrokov, Martin Ellguth, German Castro, Juan Rubiño-Zuazo, and Daryl Crozier for their continuous collaboration and discussions, M.B. Babanly, K.A. Kokh for supplying the bulk single crystal samples. We also thank Frank Wei for technical support. HLM thanks the staff of the ESRF and APS for their hospitality and support during his visit in Grenoble and Argonne. Use of the Advanced Photon Source, an Office of Science User Facility operated for the U.S. Department of Energy (DOE) Office of Science by Argonne National Laboratory, was supported by the U.S. DOE under Contract No. DE-AC02-06CH11357. Especially we thank Jürgen Kirschner and Stuart S.P. Parkin for their support and scientific discussions.

Conflict of Interest

The authors declare no conflict of interest.

Keywords

angular resolved photoemission, momentum microscopy, spin resolved photoemission, surface X-ray diffraction, topological insulators

Received: February 22, 2018

Revised: April 17, 2018

Published online:

[1] P. P. J. Haazen, J.-B. Laloe, T. J. Nummy, H. J. M. Swagten, P. Jarillo-Herrero, D. Heiman, J. S. Moodera, *Appl. Phys. Lett.* **2012**, *100*, 082404.

- [2] F. Yang, Y. R. Song, H. Li, K. F. Zhang, X. Yao, C. Liu, D. Qian, C. L. Gao, J.-F. Jia, *Phys. Rev. Lett.* **2013**, *111*, 176802.
- [3] M. G. Vergniory, M. M. Otrokov, D. Thonig, M. Hoffmann, I. V. Maznichenko, M. Geilhufe, X. Zubizarreta, S. Ostanin, A. Marmodoro, J. Henk, W. Hergert, I. Mertig, E. V. Chulkov, A. Ernst, *Phys. Rev. B* **2014**, *89*, 165202.
- [4] Z. Liu, X. Wei, J. Wang, H. Pan, F. Ji, F. Xi, J. Zhang, T. Hu, S. Zhang, Z. Jiang, W. Wen, Y. Huang, M. Ye, Z. Yang, S. Qiao, *Phys. Rev. B* **2014**, *90*, 094107.
- [5] W. Liu, D. West, L. He, Y. Xu, J. Liu, K. Wang, Y. Wang, G. van der Laan, R. Zhang, S. Zhang, K. L. Wang, *ACS Nano* **2015**, *9*, 10237.
- [6] C.-Z. Chang, P. Tang, Y.-L. Wang, X. Feng, K. Li, Z. Zhang, Y. Wang, L.-L. Wang, X. Chen, C. Liu, W. Duan, K. He, X.-C. Ma, Q.-K. Xue, *Phys. Rev. Lett.* **2014**, *112*, 056801.
- [7] A. I. Figueroa, G. van der Laan, L. J. Collins-McIntyre, G. Cibin, A. J. Dent, T. Hesjedal, *J. Phys. Chem. C* **2015**, *119*, 17344.
- [8] A. I. Figueroa, G. van der Laan, L. J. Collins-McIntyre, S.-L. Zhang, A. A. Baker, S. E. Harrison, P. Schönherr, G. Cibin, T. Hesjedal, *Phys. Rev. B* **2014**, *90*, 134402.
- [9] A. A. Baker, A. I. Figueroa, K. Kummer, L. J. Collins-McIntyre, T. Hesjedal, G. van der Laan, *Phys. Rev. B* **2015**, *92*, 094420.
- [10] Z. Liu, X. Wei, J. Wang, H. Pan, F. Ji, M. Ye, Z. Yang, S. Qiao, *Phys. Rev. B* **2015**, *92*, 100101.
- [11] M. Ye, W. Li, S. Zhu, Y. Takeda, Y. Saitoh, Y. Wang, H. Pan, M. Nurmamat, K. Sumida, F. Ji, Z. Liu, H. Yang, Z. Liu, D. Shen, A. Kimura, S. Qiao, X. Xie, *Nat. Commun.* **2015**, *6*, 1.
- [12] L. J. Collins-McIntyre, S. E. Harrison, P. Schönherr, N.-J. Steinke, C. J. Kinane, T. R. Charlton, D. Alba-Venero, A. Pushp, A. J. Kellock, S. S. P. Parkin, J. S. Harris, S. Langridge, G. van der Laan, T. Hesjedal, *EPL (Europhys. Lett.)* **2014**, *107*, 57009.
- [13] J. Henk, M. Flieger, I. V. Maznichenko, I. Mertig, A. Ernst, S. V. Eremeev, E. V. Chulkov, *Phys. Rev. Lett.* **2012**, *109*, 076801.
- [14] J. Henk, M. Flieger, I. V. Maznichenko, I. Mertig, A. Ernst, S. V. Eremeev, E. V. Chulkov, *Phys. Rev. Lett.* **2012**, *109*, 076801.
- [15] S. Roy, H. L. Meyerheim, A. Ernst, K. Mohseni, C. Tusche, M. G. Vergniory, T. V. Menshchikova, M. M. Otrokov, A. G. Ryabishchenkova, Z. S. Aliev, M. B. Babanly, K. A. Kokh, O. E. Tereshchenko, E. V. Chulkov, J. Schneider, J. Kirschner, *Phys. Rev. Lett.* **2014**, *113*, 116802.
- [16] S. Roy, H. L. Meyerheim, K. Mohseni, A. Ernst, M. M. Otrokov, M. G. Vergniory, G. Mussler, J. Kampmeier, D. Grützmacher, C. Tusche, J. Schneider, E. V. Chulkov, J. Kirschner, *Phys. Rev. B* **2014**, *90*, 155456.
- [17] A. Polyakov, H. L. Meyerheim, E. Daryl Crozier, R. A. Gordon, K. Mohseni, S. Roy, A. Ernst, M. G. Vergniory, X. Zubizarreta, M. M. Otrokov, E. V. Chulkov, J. Kirschner, *Phys. Rev. B* **2015**, *92*, 045423.
- [18] R. Shokri, H. L. Meyerheim, S. Roy, K. Mohseni, A. Ernst, M. M. Otrokov, E. V. Chulkov, J. Kirschner, *Phys. Rev. B* **2015**, *91*, 205430.
- [19] M. v. Laue, *Ann. d Physik* **1936**, *26*, 55.
- [20] I. K. Robinson, *Phys. Rev. B* **1986**, *33*, 3830.
- [21] M. P. Seah, W. A. Dench, *Surf. Interface Anal.* **1979**, *1*, 2.
- [22] A. Winkelmann, A. A. Ünal, C. Tusche, M. Ellguth, C.-T. Chiang, J. Kirschner, *New J. Phys.* **2012**, *14*, 083027.
- [23] S. Moser, *J. Electron Spectrosc. Relat. Phenom.* **2017**, *214*, 29.
- [24] C. Tusche, A. Krasnyuk, J. Kirschner, *Ultramicroscopy* **2015**, *159*, 520.
- [25] C. Tusche, M. Ellguth, A. A. Ünal, C.-T. Chiang, A. Winkelmann, A. Krasnyuk, M. Hahn, G. Schönhense, J. Kirschner, *Appl. Phys. Lett.* **2011**, *99*, 032505.
- [26] D. Vasilyev, C. Tusche, F. Giebels, H. Gollisch, R. Feder, J. Kirschner, *J. Electron Spectrosc. Relat. Phenom.* **2015**, *199*, 10.

- [27] C. Tusche, M. Ellguth, A. Krasnyuk, A. Winkelmann, D. Kutnyakhov, P. Lushchik, K. Medjanik, G. Schönense, J. Kirschner, *Ultramicroscopy* **2013**, 130, 70.
- [28] S. Nakajima, *J. Phys. Chem. Solids* **1963**, 24, 479.
- [29] H. Gobrecht, K.-E. Boeters, G. Pantzer, *Z. Phys.* **1964**, 177, 68.
- [30] C. P. Vicente, J. L. Tirado, K. Adouby, J. C. Jumas, A. Abba Tour, G. Kra, *Inorg. Chem.* **1999**, 38, 2131.
- [31] V. V. Atuchin, V. A. Golyashov, K. A. Kokh, I. V. Korolkov, A. S. Kozhukhov, V. N. Kruchinin, S. V. Makarenko, L. D. Pokrovsky, I. P. Prosvirin, K. N. Romanyuk, O. E. Tereshchenko, *Cryst. Growth Des.* **2011**, 11, 5507.
- [32] X. He, W. Zhou, Z. Y. Wang, Y. N. Zhang, J. Shi, R. Q. Wu, J. A. Yarmoff, *Phys. Rev. Lett.* **2013**, 110, 156101.
- [33] N. Fukui, T. Hirahara, T. Shirasawa, T. Takahashi, K. Kobayashi, S. Hasegawa, *Phys. Rev. B* **2012**, 85, 115426.
- [34] D. D. dos Reis, L. Barreto, M. Bianchi, G. A. S. Ribeiro, E. A. Soares, W. S. Silva, V. E. de Carvalho, J. Rawle, M. Hoesch, C. Nicklin, W. P. Fernandes, J. Mi, B. B. Iversen, P. Hofmann, *Phys. Rev. B* **2013**, 88, 041404.
- [35] I. K. Robinson, D. J. Tweet, *Rep. Prog. Phys.* **1992**, 55, 599.
- [36] H. L. Meyerheim, W. Moritz, *Appl. Phys. A* **1998**, 67, 645.
- [37] C. Schamper, H. L. Meyerheim, W. Moritz, *J. Appl. Crystallogr.* **1993**, 26, 687.
- [38] C. M. Schlepütz, R. Herger, P. R. Willmott, B. D. Patterson, O. Bunk, Ch. Brönnimann, B. Henrich, G. Hülsen, E. F. Eikenberry, *Acta Crystallogr. A* **2005**, 61, 418.
- [39] E. Vlieg, *J. Appl. Crystallogr.* **1997**, 30, 532.
- [40] W. F. Kuhs, *Acta Cryst. A* **1992**, 48, 80.
- [41] M. J. Buerger, *Kristallographie. Eine Einführung in die geometrische und röntgenographische Kristallkunde*, Vol. 9, Walter de Gruyter Verlag, Berlin **1977**.
- [42] $R_u = \sum |F_{\text{obs}}| - |F_{\text{calc}}| / \sum |F_{\text{obs}}|$. Here, F_{obs} , F_{calc} are the experimental and calculated structure factors, respectively. The summation runs over all datapoints.
- [43] S. C. Abrahams, *Acta Crystallogr. A* **1969**, 25, 165.
- [44] I. K. Robinson, in *Handbook on Synchrotron Radiation*, Vol. 3 (Eds: G. S. Brown, D. E. Moncton), North Holland: Amsterdam, New York, Oxford **1991**, Ch. 7, pp. 221–266.
- [45] S. H. Kim, H. L. Meyerheim, J. Barthel, J. Kirschner, J. Seo, J.-S. Kim, *Phys. Rev. B* **2005**, 71, 205418.
- [46] Z.-H. Zhu, G. Levy, B. Ludbrook, C. N. Veenstra, J. A. Rosen, R. Comin, D. Wong, P. Dosanjh, A. Ubaldini, P. Syers, N. P. Butch, J. Paglione, I. S. Elfimov, A. Damascelli, *Phys. Rev. Lett.* **2011**, 107, 186405.
- [47] H. M. Benia, C. Lin, K. Kern, C. R. Ast, *Phys. Rev. Lett.* **2011**, 107, 177602.
- [48] P. D. C. King, R. C. Hatch, M. Bianchi, R. Ovsyannikov, C. Lupulescu, G. Landolt, B. Slomski, J. H. Dil, D. Guan, J. L. Mi, E. D. L. Rienks, J. Fink, A. Lindblad, S. Svensson, S. Bao, G. Balakrishnan, B. B. Iversen, J. Osterwalder, W. Eberhardt, F. Baumberger, Ph. Hofmann, *Phys. Rev. Lett.* **2011**, 107, 096802.
- [49] M. Bianchi, R. C. Hatch, J. Mi, B. B. Iversen, P. Hofmann, *Phys. Rev. Lett.* **2011**, 107, 086802.
- [50] T. Valla, Z.-H. Pan, D. Gardner, Y. S. Lee, S. Chu, *Phys. Rev. Lett.* **2012**, 108, 117601.
- [51] M. S. Bahramy, P. D. C. King, A. De La Torre, J. J. Chang, M. Shi, L. Patthey, G. Balakrishnan, Ph. Hofmann, R. Arita, N. Nagaosa, F. Baumberger, *Nat. Commun.* **2012**, 3, 1159.
- [52] M. Bianchi, R. C. Hatch, Z. Li, P. Hofmann, F. Song, J. Mi, B. B. Iversen, Z. M. Abd El-Fattah, P. Löptien, L. Zhou, A. A. Khajetoorians, J. Wiebe, R. Wiesendanger, J. W. Well, *ACS Nano* **2012**, 6, 7009.
- [53] M. Z. Hasan, C. L. Kane, *Rev. Mod. Phys.* **2010**, 82, 3045.
- [54] L. Fu, C. L. Kane, E. J. Mele, *Phys. Rev. Lett.* **2007**, 98, 106803.
- [55] L. Fu, C. L. Kane, *Phys. Rev. Lett.* **2008**, 100, 096407.
- [56] S. Suga, C. Tusche, *J. Electron Spectrosc. Relat. Phenom.* **2015**, 200, 119142.
- [57] D. Hsieh, Y. Xia, L. Wray, D. Qian, A. Pal, J. H. Dil, J. Osterwalder, F. Meier, G. Bihlmayer, C. L. Kane, Y. S. Hor, R. J. Cava, M. Z. Hasan, *Science* **2009**, 323, 919.
- [58] D. Hsieh, Y. Xia, D. Qian, L. Wray, J. H. Dil, F. Meier, J. Osterwalder, L. Patthey, J. G. Checkelsky, N. P. Ong, A. V. Fedorov, H. Lin, A. Bansil, D. Grauer, Y. S. Hor, R. J. Cava, M. Z. Hasan, *Nature* **2009**, 460, 1101.
- [59] C.-H. Park, S. G. Louie, *Phys. Rev. Lett.* **2012**, 109, 097601.
- [60] Y. Cao, J. A. Waugh, N. C. Plumb, T. J. Reber, S. Parham, G. Landolt, Z. Xu, A. Yang, J. Schneeloch, G. Gu, J. H. Dil, D. S. Dessau, **2013**, arXiv:1211.5998.
- [61] C. Jozwiak, C.-H. Park, K. Gotlieb, C. Hwang, D.-H. Lee, S. G. Louie, J. D. Denlinger, C. R. Rotundu, R. J. Birgeneau, Z. Hussain, A. Lanzara, *Nat. Phys.* **2013**, 9, 293.
- [62] Q.-K. Xue, *Nat. Phys.* **2013**, 9, 265.
- [63] J. Sánchez-Barriga, A. Varykhalov, J. Braun, S.-Y. Xu, N. Alidoust, O. Kornilov, J. Minár, K. Hummer, G. Springholz, G. Bauer, R. Schumann, L. V. Yashina, H. Ebert, M. Z. Hasan, O. Rader, *Phys. Rev. X* **2014**, 4, 011046.
- [64] Z. Xie, S. He, C. Chen, Y. Feng, H. Yi, A. Liang, L. Zhao, D. Mou, J. He, Y. Peng, X. Liu, Y. Liu, G. Liu, X. Dong, L. Yu, J. Zhang, S. Zhang, Z. Wang, F. Zhang, F. Yang, Q. Peng, X. Wang, C. Chen, Z. Xu, X. J. Zhou, *Nat. Commun.* **2014**, 5, 3382.
- [65] C. Tusche, P. Goslawski, D. Kutnyakhov, M. Ellguth, K. Medjanik, H. J. Elmers, S. Chernov, R. Wallauer, D. Engel, A. Jankowiak, G. Schönense, *Appl. Phys. Lett.* **2016**, 108, 261602.
- [66] S. V. Chernov, K. Medjanik, C. Tusche, D. Kutnyakhov, S. A. Nepijko, A. Oelsner, J. Braun, J. Minár, S. Borek, H. Ebert, H. J. Elmers, J. Kirschner, G. Schnhense, *Ultramicroscopy* **2015**, 159, 453.
- [67] G. Schönense, *Phys. Scr.* **1990**, T31, 255.
- [68] H. Bentmann, H. Maaß, E. E. Krasovskii, T. R. F. Peixoto, C. Seibel, M. Leandersson, T. Balasubramanian, F. Reinert, *Phys. Rev. Lett.* **2017**, 119, 106401.
- [69] E. Tamura, W. Piepke, R. Feder, *Phys. Rev. Lett.* **1987**, 59, 934.
- [70] H. Maaß, H. Bentmann, C. Seibel, C. Tusche, S. V. Ereemeev, T. R. F. Peixoto, O. E. Tereshchenko, K. A. Kokh, E. V. Chulkov, J. Kirschner, F. Reinert, *Nat. Commun.* **2016**, 7, 11621.
- [71] S. M. Grivin, R. E. Prange, K. v. Klitzing, editors, *The Quantum Hall Effect*. Springer Verlag, Berlin, Heidelberg, New York **1986**.
- [72] B. Andrei Bernevig, T. L. Hughes, S.-C. Zhang, *Science* **2006**, 314, 1757.
- [73] M. König, S. Wiedmann, C. Brüne, A. Roth, H. Buhmann, L. W. Molenkamp, X.-L. Qi, S.-C. Zhang, *Science* **2007**, 318, 766.
- [74] S. Murakami, *Phys. Rev. Lett.* **2006**, 97, 236805.
- [75] M. Wada, S. Murakami, F. Freimuth, G. Bihlmayer, *Phys. Rev. B* **2011**, 83, 121310.
- [76] T. Hirahara, G. Bihlmayer, Y. Sakamoto, M. Yamada, H. Miyazaki, S.-i. Kimura, S. Blügel, S. Hasegawa, *Phys. Rev. Lett.* **2011**, 107, 166801.
- [77] M. Chen, J.-P. Peng, H.-M. Zhang, L.-L. Wang, K. He, X.-C. Ma, Q.-K. Xue, *Appl. Phys. Lett.* **2012**, 101, 081603.
- [78] F. Yang, L. Miao, Z. F. Wang, M.-Y. Yao, F. Zhu, Y. R. Song, M.-X. Wang, J.-P. Xu, A. V. Fedorov, Z. Sun, G. B. Zhang, C. Liu, F. Liu, D. Qian, C. L. Gao, J.-F. Jia, *Phys. Rev. Lett.* **2012**, 109, 016801.
- [79] S. H. Kim, K.-H. Jin, J. Park, J. S. Kim, S.-H. Jhi, T.-H. Kim, H. W. Yeom, *Phys. Rev. B* **2014**, 89, 155436.
- [80] C. Sabater, D. Gosálbez-Martínez, J. Fernández-Rossier, J. G. Rodrigo, C. Untiedt, J. J. Palacios, *Phys. Rev. Lett.* **2013**, 110, 176802.
- [81] I. K. Drozdov, A. Alexandradinata, S. Jeon, S. Nadj-Perge, H. Ji, R. J. Cava, B. Andrei Bernevig, A. Yazdani, *Nat. Phys.* **2014**, 10, 664.

- [82] O. Waldmann, B. Ludewigt, *Rev. Sci. Instrum.* **2011**, *82*, 113505.
- [83] H. Mönig, J. Sun, Yu. M. Koroteev, G. Bihlmayer, J. Wells, E. V. Chulkov, K. Pohl, Ph. Hofmann, *Phys. Rev. B* **2005**, *72*, 085410.
- [84] Ph. Hofmann, *Prog. Surf. Sci.* **2006**, *81*, 191.
- [85] S. H. Su, P. Y. Chuang, S. W. Chen, H. Y. Chen, Y. Tung, W.-C. Chen, C.-H. Wang, Y.-W. Yang, J. C. A. Huang, T.-R. Chang, H. Lin, H.-T. Jeng, C.-M. Cheng, K.-D. Tsuei, H. L. Su, Y. C. Wu, *Chem. Mater.* **2017**, *29*, 8992.
- [86] K. AU Ishizaka, M. S. Bahramy, H. Murakawa, M. Sakano, T. Shimojima, T. Sonobe, K. Koizumi, S. Shin, H. Miyahara, A. Kimura, K. Miyamoto, T. Okuda, H. Namatame, M. Taniguchi, R. Arita, N. Nagaosa, K. Kobayashi, Y. Murakami, R. Kumai, Y. Kaneko, Y. Onose, Y. Tokura, *Nat. Mater.* **2011**, *10*, 521.
- [87] B. K. Teo, D. C. Joy (Eds.), *EXAFS Spectroscopy*. Plenum Press, New York **1981**.
- [88] B. K. Teo, *EXAFS: Basic Principles and Data Analysis*, Vol. 9 of Inorganic Chemistry Concepts, Springer Verlag, Berlin, Heidelberg, New York **1986**.
- [89] D. C. Koningsberger, R. Prins, editors, *X-Ray Absorption: Principles, Applications, Techniques of EXAFS, SEXAFS and XANES*. Wiley, New York **1988**.
- [90] H. Fricke, *Phys. Rep.* **1920**, *16*, 202.
- [91] G. Hertz, *Z. Phys.* **1920**, *3*, 19.
- [92] R. L. Kronig, *Z. Phys.* **1931**, *70*, 317.
- [93] D. Sayers, E. Stern, F. Lytle, *Phys. Rev. Lett.* **1971**, *27*, 1204.
- [94] E. Stern, B. Bunker, S. Heald, *Phys. Rev. B* **1980**, *21*, 5521.
- [95] P. H. Citrin, *Phys. Rev. B* **1985**, *31*, 700.
- [96] T. Ressler, *J. Synchr. Radiat.* **1998**, *5*, 118.
- [97] The unweighted residuum (R_u) is defined by: $R_u = \sum [(Y_{i_{obs}} - Y_{i_{calc}}) / \sum (Y_{i_{obs}})]$, where $Y_{i_{obs}}$ and $Y_{i_{calc}}$ are the experimental and calculated magnitudes of the peak selected in the FT of the $\chi(k)$ spectrum and the summation extends over all points (i) in the window used to filter the peak.
- [98] Y. L. Chen, J.-H. Chu, J. G. Analytis, Z. K. Liu, K. Igarashi, H.-H. Kuo, X. L. Qi, S. K. Mo, R. G. Moore, D. H. Lu, M. Hashimoto, T. Sasagawa, S. C. Zhang, I. R. Fisher, Z. Hussain, Z. X. Shen, *Science* **2010**, *329*, 659.
- [99] M. G. Vergniory, M. M. Otrokov, D. Thonig, M. Hoffmann, I. V. Maznichenko, M. Geilhufe, X. Zubizarreta, S. Ostanin, A. Marmodoro, J. Henk, W. Hergert, I. Mertig, E. V. Chulkov, A. Ernst, *Phys. Rev. B* **2014**, *89*, 165202.
- [100] L. Andrew Wray, S.-Y. Xu, Y. Xia, D. Hsieh, A. V. Fedorov, Y. S. Hor, R. J. Cava, A. Bansil, H. Lin, M. Zahid Hasan, *Nat. Phys.* **2011**, *7*, 32.
- [101] M. M. Otrokov, E. V. Chulkov, A. Arnau, *Phys. Rev. B* **2015**, *92*, 165309.
- [102] P. Sessi, R. R. Biswas, T. Bathon, O. Storz, S. Wilfert, A. Barla, K. A. Kohk, O. E. Tereshchenko, K. Fauth, M. Bode, A. V. Balatsky, *Nat. Commun.* **2016**, *7*, 12027.
- [103] Z.-H. Zhu, G. Levy, B. Ludbrook, C. N. Veenstra, J. A. Rosen, R. Comin, D. Wong, P. Dosanjh, A. Ubaldini, P. Syers, N. P. Butch, J. Paglione, I. S. Elfimov, A. Damascelli, *Phys. Rev. Lett.* **2011**, *107*, 186405.
- [104] P. D. C. King, R. C. Hatch, M. Bianchi, R. Ovsyannikov, C. Lupulescu, G. Landolt, B. Slomski, J. H. Dil, D. Guan, J. L. Mi, E. D. L. Rienks, J. Fink, A. Lindblad, S. Svensson, S. Bao, G. Balakrishnan, B. B. Iversen, J. Osterwalder, W. Eberhardt, F. Baumberger, Ph. Hofmann, *Phys. Rev. Lett.* **2011**, *107*, 096802.
- [105] L. Miao, Z. F. Wang, W. Ming, M.-Y. Yao, M. Wang, F. Yang, Y. R. Song, F. Zhu, A. V. Fedorov, Z. Sun, C. L. Gao, C. Liu, Q.-K. Xue, C.-X. Liu, F. Liu, D. Qian, J.-F. Jia, *Proc. Natl. Acad. Sci. USA* **2013**, *110*, 2758.
- [106] T. V. Menshchikova, M. M. Otrokov, S. S. Tsirkin, D. A. Samorokov, V. V. Bebnava, A. Ernst, V. M. Kuznetsov, E. V. Chulkov, *Nano Lett.* **2013**, *13*, 6064.
- [107] J. Sanchez-Barriga, A. Varykhalov, G. Springholz, H. Steiner, R. Kirchschrager, G. Bauer, O. Caha, E. Schierle, E. Weschke, A. A. Unal, S. Valencia, M. Dunst, J. Braun, H. Ebert, J. Minar, E. Golias, L. V. Yashina, A. Ney, V. Holy, O. Rader, *Nat. Commun.* **2016**, *7*, 10559.
- [108] R. R. Biswas, A. V. Balatsky, *Phys. Rev. B* **2010**, *81*, 233405.
- [109] A. M. Black-Schaffer, A. V. Balatsky, *Phys. Rev. B* **2012**, *85*, 121103.
- [110] A. M. Black-Schaffer, A. V. Balatsky, *Phys. Rev. B* **2012**, *86*, 115433.
- [111] A. Polyakov, C. Tusche, M. Ellguth, E. D. Crozier, K. Mohseni, M. M. Otrokov, X. Zubizarreta, M. G. Vergniory, M. Geilhufe, E. V. Chulkov, A. Ernst, H. L. Meyerheim, S. S. P. Parkin, *Phys. Rev. B* **2017**, *95*, 180202.
- [112] M. Lüders, A. Ernst, W. M. Temmerman, Z. Szotek, P. J. Durham, *J. Phys.: Condens. Matter* **2001**, *13*, 8587.
- [113] M. Geilhufe, S. Achilles, M. A. Köbis, M. Arnold, I. Mertig, W. Hergert, A. Ernst, *J. Phys.: Condens. Matter* **2015**, *27*, 435202.
- [114] P. Soven, *Phys. Rev.* **1967**, *156*, 809.